Non-Reducing Proteomics Reveals Disulfide-dependent Proteoform Remodeling Under Oxidative Stress

Authors

Yeonjoo Lee, Tae-Kyung Kim, Seungjin Na, Kong-Joo Lee, Jaeho Jeong, and Eun Joo Song

Correspondence

kjl@ewha.ac.kr; jaeho.jeong@cj.net; esong@ewha.ac.kr

In Brief

We combined non-reducing tandem mass tag (TMT) proteomics with LC–MS metabolomics to investigate oxidative stress responses in MDA-MB-231 cells. This approach revealed multiple previously undetectable redox-sensitive secondary protein bands and enabled mapping of protein disulfide networks with DBond, a new algorithm for automated detection of disulfide-linked peptides. Sequence-level analysis showed isoform-specific cysteine linkages with distinct local motifs, while metabolomics demonstrated coordinated rewiring of major pathways driven by redox-sensitive enzymes.

Graphical Abstract

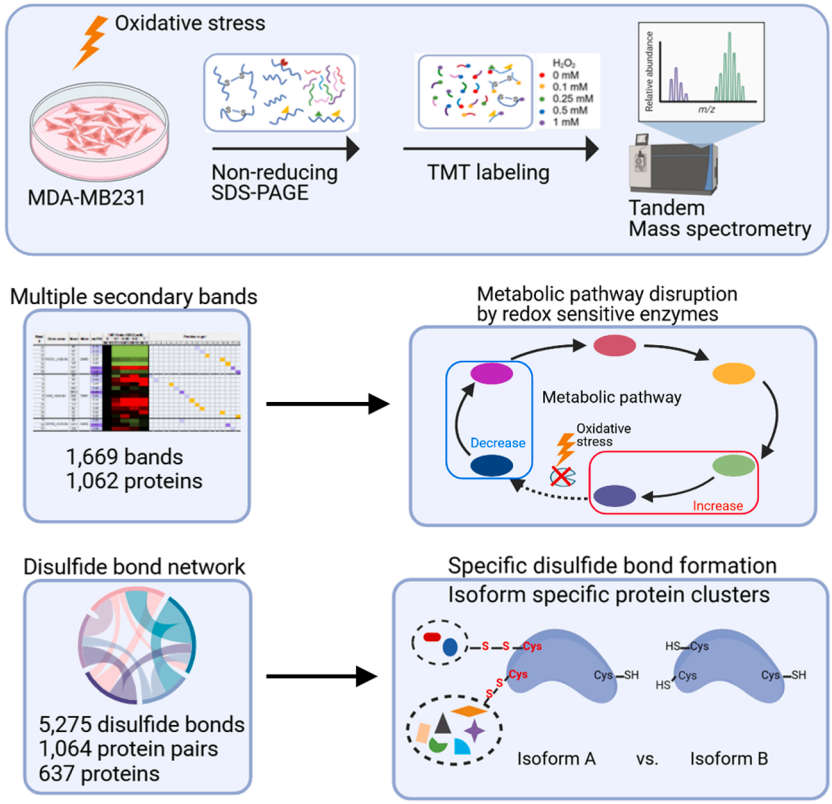

Highlights

- Non-reducing TMT proteomics detects redox-sensitive protein bands.
- Integrated omics reveals redox-driven metabolic pathway rewiring.
- DBond algorithm maps protein disulfide bond networks comprehensively.
- Isoform-specific disulfide cysteines enriched in local sequence motifs.

2026, Mol Cell Proteomics *25(4)*, 101548

https://doi.org/10.1016/j.mcpro.2026.101548

Non-Reducing Proteomics Reveals Disulfide-dependent Proteoform Remodeling Under Oxidative Stress

Yeonjoo Lee[1], Tae-Kyung Kim[2], Seungjin Na[3], Kong-Joo Lee[1,*], Jaeho Jeong[2,*], and Eun Joo Song[1,4,*]

Oxidative stress triggers redox-sensitive post-translational modifications, notably disulfide bond formation involving cysteine residues. However, these bonds are often overlooked in proteomics due to the routine use of reducing agents. Here, we employed (LC-MS based metabolomics and non-reducing tandem mass tag proteomics to investigate the effects of hydrogen peroxide on MDA-MB-231 cells. Metabolomic analysis revealed pathway-specific inhibition of major metabolic pathways including glycolysis, the tricarboxylic acid cycle, and nucleotide biosynthesis. Proteomic analysis using the DBond algorithm revealed extensive and isoform-specific disulfide crosslinks across more than 1000 proteins. These linkages were enriched at redox-sensitive cysteines near basic residues and displayed high isoform specificity. Our findings demonstrate that disulfide bond formation serves as a selective mechanism of redox regulation. This study highlights the utility of non-reducing proteomics in elucidating redox-controlled protein networks and structural dynamics under oxidative stress.

Hydrogen peroxide (H_2O_2), a reactive oxygen species (ROS), is produced by non-phagocytic cells in response to various stimuli and functions as a second messenger regulating cellular processes such as proliferation, differentiation, inflammation, stress responses, aging, and cell death (1, 2). These effects are mediated by redox modifications of cysteine (Cys) residues in regulatory proteins including PTEN, protein tyrosine phosphatases, peroxiredoxins (PRDXs), Hsp33, and EGFR (1, 3–5). Oxidation of reactive Cys thiols serves as a molecular switch that alters protein structure, catalytic activity and protein-protein interactions. Redox sensitivity of Cys residues is strongly influenced by the local microenvironment and thiol pKa (6–8).

Cys thiols (Cys–SH) can undergo diverse oxidative modifications, both reversible and irreversible. These include sulfenic acid (Cys–SOH), disulfide bonds (Cys–S–S–Cys), sulfinic acid (Cys–SO_2H), and sulfonic acid (Cys–SO_3H) (9–11). Variations in reversibility among Cys modifications mean that different H_2O_2 levels result in different oxidative forms, and thereby distinct biological effects. While basal levels of H_2O_2 (<100 μM) support physiological signaling, higher levels (>200 μM) are associated with oxidative stress or apoptosis. Among these modifications, disulfide bonds are particularly important because they are reversible and function as key structural determinants. However, they are frequently overlooked in proteomics workflows that employ reducing agents such as DTT or β-mercaptoethanol (12, 13). These treatments eliminate disulfide linkages that are dynamically regulated and reversibly modulated by redox state.

Isoform-specific examples illustrate the selectivity of disulfide-dependent regulation. Nm23-H1, for example, forms an intramolecular disulfide bond upon ROS exposure, leading to structural rearrangements and altered activity. In contrast, its isoform Nm23-H2 lacks the requisite Cys for the disulfide formation and remains unresponsive to oxidation. Similar redox selectivity has been observed in other proteins such as GAPDH, peroxiredoxin 1 (PRDX1), and DJ-1. GAPDH undergoes conformation changes that reprogram binding partners. PRDX1 oxidation induces structural remodeling and altered activity, while disulfide linkages stabilize DJ-1 structure (6–8, 14–17). Selective thiol-labeling probes such as NPSB-1 have further demonstrated that Cys reactivity differs depending on local structural context, highlighting the need for approaches that preserve native disulfide linkages (13). These examples show that disulfide formation is not a random byproduct of oxidative stress. Instead, it represents a selective and structurally defined mechanism of redox regulation.

From the [1]College of Pharmacy and Graduate School of Pharmaceutical Sciences, Ewha Womans University, Republic of Korea; [2]CJ BIO R&QE, CJ CheilJedang, Suwon, Republic of Korea; [3]Digital Omics Research Center, Korea Basic Science Institute, Cheongju, Republic of Korea; and [4]Graduate Program in Innovative Biomaterials Convergence, Ewha Womans University, Seoul, Republic of Korea
*For correspondence: Kong-Joo Lee, kjl@ewha.ac.kr; Jaeho Jeong, jaeho.jeong@cj.net; Eun Joo Song, esong@ewha.ac.kr.

https://doi.org/10.1016/j.mcpro.2026.101548

To overcome the limitation in detecting disulfide linkages, we implemented a non-reducing tandem mass tag (TMT)-based proteomics workflow combined with LC-MS-based metabolomics in H_2O_2-treated MDA-MB-231 breast cancer cells (8). Nonreducing SDS–PAGE was used to separate isoforms of redox-sensitive proteins under conditions that minimize disruption of native disulfide bonds and redox states. A key component of this strategy is the DBond algorithm, which enables precise identification of intra- and interprotein disulfide-linked peptides directly from tandem mass spectra (12). Integrating these approaches revealed widespread disulfide crosslinking, highlighting disulfide formation as a selective and dynamic redox regulation in cancer cells. These findings reveal that disulfide bonding is a selective mechanism of redox regulation and show that non-reducing proteomics with DBond algorithm can clarify oxidative stress-responsive protein networks.

EXPERIMENTAL PROCEDURES

This study aimed to elucidate redox-dependent disulfide bond formation and associated metabolic responses in MDA-MB-231 breast cancer cells exposed to oxidative stress. Cells were treated with H_2O_2 at five concentrations (0, 0.1, 0.25, 0.5 and 1 mM) for 1 h. We applied an integrated approach combining LC-MS-based metabolomics and TMT-based non-reducing proteomics. Disulfide bonds were preserved through non-reducing SDS-PAGE and identified using the DBond algorithm. Changes in metabolic pathway activity and redox-sensitive protein isoforms were quantitatively assessed.

Cell Culture

MDA-MB-231 cells were cultured in MEM alpha (CM054–050) from GenDEPOT, supplemented with 10% fetal bovine serum and penicillin/streptomycin (Sigma) at 37 °C with 5% CO_2.

Sample Preparation for Metabolomics

For metabolomics analysis, we utilized the two-step method as previously described (18). MDA-MB-231 cells were treated with 0, 0.1, 0.25, 0.5, and 1 mM H_2O_2 in Hank's Balanced Salt Solution for 1 h (n = 5 per concentration). Following treatment, cells were washed with PBS, and then their metabolites were extracted using 1 ml of cold 60% methanol and collected by scraping. For normalization, DNA concentrations were measured using a Nanodrop. After adding 400 μl of chloroform to each sample, cells were vortexed twice for 10 s each and centrifuged at 4000 rpm for 10 min at 4 °C. The supernatant from the upper hydrophilic layer was transferred to an Amicon Ultra 3K 0.5 ml centrifugal filter (Merck) and centrifuged at 13,000×*g* for 1 h at 4 °C to remove macromolecules including proteins. The filtrate was then concentrated using a vacuum concentrator and analyzed using Mass spectrometry.

Redox-Sensitive Metabolite Profiling Using Mass Spectrometry

MS spectrometry was performed using an Acquity UPLC I-class system coupled with Q-Tof mass spectrometers (Xevo G2-XS, Waters Co.) for intracellular metabolites. Two different columns and mobile phases were used depending on the ionization mode.

For negative ion mode, intracellular metabolites were analyzed using an Acquity UPLC HSS T3 column (2.1 × 150 mm, 1.8 μm, Waters Co.). The mobile phases consisted of 0.01 M tributylamine/0.02 M acetic acid in distilled water (A) and methanol (B). The total flow rate was 0.3 ml/min. The LC gradient program started with 2% B, held for 5 min, then increased to 80% B at 30 min, held for 2 min, and returned to 2% B at 32.1 min. The column was conditioned for another 3.9 min, resulting in a total run time of 36 min. The injection volume was 5 μl, and the oven temperature was set to 40 °C. Mass spectral data were acquired in negative electrospray ionization mode with a capillary voltage of 1.2 kV, cone voltage of 40 V, source temperature of 120 °C, and cone gas and desolvation gas flow rates of 40 and 800 L/h, respectively.

For positive ion mode, intracellular metabolites were analyzed using an Intrada Amino Acid column (2.0 × 150 mm, 3 μm, Imtakt Co., Japan). The mobile phases consisted of 0.3% formic acid in acetonitrile (A) and 0.08 M ammonium formate in 20% acetonitrile (B). The total flow rate was 0.35 ml/min. The LC gradient program started with 20% B, held for 5 min, then increased to 100% B at 14 min, held for 2 min, and returned to 20% B at 16.1 min. The column was conditioned for another 3.9 min, resulting in a total run time of 20 min. The injection volume was 5 μl, and the oven temperature was set to 35 °C. Mass spectral data were acquired in positive electrospray ionization mode with a capillary voltage of 2.5 kV, cone voltage of 30 V, source temperature of 100 °C, and cone gas and desolvation gas flow rates of 20 and 400 L/h, respectively.

Sample Preparation for Proteomics

For proteomics analysis, MDA-MB-231 cells were treated with 0, 0.1, 0.25, 0.5, and 1 mM H_2O_2 in Hank's Balanced Salt Solution buffer for 1 h. The cells were then washed with PBS and lysed in RIPA buffer (50 mM Tris, 150 mM NaCl, 0.1% SDS, 0.5% deoxycholate, 1% NP 40, pH 8.0) supplemented with protease inhibitor (Roche) and 1 mM sodium orthovanadate.

To minimize artifactual thiol-disulfide exchange or disulfide reshuffling during extraction, cell lysates were prepared rapidly on ice, and all steps from lysis to centrifugation were completed within 30 min. In the subsequent data analysis, only disulfide-linked peptide pairs that met stringent filtering criteria-including high DBond scores, a minimum peptide length for both linked partners, and consistent detection across the same protein pair-were included in the final dataset. These criteria were applied to increase confidence in disulfide assignment, although they cannot completely exclude products arising from side reactions.

We also note that disulfide linkages proximal to basic residues may be preferentially identified due to enhanced fragmentation efficiency under collision-induced dissociation conditions; therefore, the resulting dataset may be biased toward such sequence contexts.

Lysates were incubated on ice for 15 min with vortexing every 5 min, then centrifuged at 14,000 rpm for 15 min at 4 °C. The protein concentration in the supernatant was measured using the BCA assay (Pierce). Each lysate was prepared with non-reducing SDS-PAGE sample buffer and boiled at 95 °C for 5 min immediately before electrophoresis.

Silver Staining

To maintain protein oxidation state, the lysates were prepared using a nonreducing SDS-PAGE sample buffer. The samples were loaded (70 μg of protein) onto a PROTEAN II xi 2-D Cell system (BIO-RAD) for separation and further analysis. The entire gel was silver stained based on the standard instructions on the PlusOne Silver Staining Kit (GE Healthcare) and divided into 18 bands.

Glutaraldehyde was omitted in the sensitizing step. Formaldehyde was present in the silver and developing solutions as per kit formulation (19).

Redox-Sensitive Proteomics Using In-Gel Digestion, Protein Quantification, and Modification Analysis with TMT Labeling and Mass Spectrometry

Gel bands were excised with a scalpel into 18 fractions based on molecular weight, destained with 15 mM potassium ferricyanide and 50 mM sodium thiosulfate. After destaining, the gel bands were washed with distilled water to completely remove the destaining reagent. The pH was adjusted to 8.0 using 200 mM triethylammonium bicarbonate buffer (TEAB) to facilitate trypsin digestion. The gels were dehydrated with acetonitrile (ACN), rehydrated with 10 to 20 μl of 25 mM TEAB containing 20 ng/μl sequencing-grade trypsin (Promega, Madison, WI,), and incubated at 37 °C for 15 to 17 h. Peptides were extracted using 30 μl of 60% ACN solution. The extracts were pooled and dried using a vacuum concentrator for MS analysis. Acid was omitted during TMT labeling to maintain a final peptide extract pH of ~8.5, optimizing labeling efficiency.

Each fraction from MDA-MB-231 was resuspended in 30 μl of TMT Dissolution Buffer (Thermo Fisher Scientific, Waltham, MA) and aminolabeled with one of the six TMT tags at 25 °C for 1 h, and subsequently pooled in equal amounts.

TMT-labeled peptides were concentrated using a vacuum concentrator and dissolved in 10% ACN containing 0.1% formic acid. The dissolved peptides were desalted on-line using a trap column (180 μm × 20 mm, Symmetry C18, Waters Co.,) prior to separation. Peptide separation was performed over 80 min on a C18 reversed-phase analytical column (75 μm × 250 mm, 1.7 μm particle size, BEH130 C18, Waters Co.) equipped with an integrated electrospray ionization PicoTip (±10 μm, New Objective). The nanoAcquity UPLC system coupled with ESI-MS (nanoLC-MS, SYNAPT G2Si HDMS, Waters Co.,) was used for analysis as described below (14).

The mobile phases consisted of 0.1% formic acid in distilled water (Solvent A) and 0.1% formic acid in ACN (Solvent B). The optimized LC gradient program began with 95% Solvent A and 5% Solvent B, held for 0.5 min, followed by a gradual increase to 40% Solvent B at 40 min and 60% Solvent B at 50 min. The gradient then reached 80% Solvent B at 60 min, held for 5 min, and returned to the initial condition of 95% Solvent A and 5% Solvent B at 70 min. The column was conditioned for an additional 10 min to ensure stability. The flow rate was maintained at 0.35 ml/min throughout the run, and the injection volume was set to 5 μl.

Mass spectrometry was performed under optimized conditions to ensure accurate and reproducible results. The instrument was operated in positive electrospray ionization mode (ES+), with a capillary voltage of 2.5 kV and a source temperature of 100 °C. The sampling cone was set to 40 eV, and the source offset was adjusted to 80 eV. The source gas flow was maintained at 0 ml/min, while the desolvation temperature was set to 250 °C. Cone gas flow and desolvation gas flow rates were set to 50 L/h and 600 L/h, respectively. Nanoflow gas pressure was maintained at 0.5 bar, purge gas flow at 600 ml/h, and nebulizer gas flow at 6.5 bar.

Mass Spectrometry Data Acquisition and Collision-Induced Dissociation Parameters (SYNAPT G2Si HDMS)

Mass spectrometric analyses were performed on a SYNAPT G2Si HDMS mass spectrometer (Waters) coupled to a nanoAcquity UPLC system and operated in positive electrospray ionization (ESI+) mode. Survey MS spectra were acquired over an m/z range of 350 to 1200, and MS/MS spectra were acquired over an m/z range of 50 to 1500.

Data-dependent acquisition was employed, in which precursor ions were selected for MS/MS when the signal intensity exceeded a threshold of 3000 counts. MS survey scans were acquired with a scan time of 0.40 s and an interscan time of 0.01 s. MS/MS scans were acquired with a scan time of 0.40 s and an interscan time of 0.01 s. Fragmentation was performed for precursor ions with charge states +2, +3, and +4 only. MS/MS acquisition was terminated and switched back to MS mode when the total ion current dropped below 1,000,000 counts or after 1.2 s (corresponding to 3 MS/MS scans), whichever occurred first.

Precursor ion selection was governed by an instrument-defined peak detection window of 3.0 m/z, which was used to define candidate precursor ions for quadrupole selection prior to fragmentation. Collision-induced dissociation was performed in the trap cell using collision energy profile mode, in which charge-state– and m/z-dependent collision energies were applied. Argon was used as the collision gas in the trap cell, with a gas flow rate of 2.0 ml/min. The transfer collision energy was maintained at the default setting of 2.0 eV.

Ion mobility separation was not enabled during data acquisition; therefore, ion mobility wave parameters were not applicable. The instrument method retained an IMS gas flow setting of 90 ml/min, but no ion mobility separation was applied during MS or MS/MS acquisition.

Database Search and Validation

Mascot (version 2.8.0) was used to search against the SwissProt human database (release 57.15, 20,233 entries). Parameters included trypsin digestion with up to one missed cleavage, precursor and fragment ion tolerance of 0.1 Da, and fixed/variable modifications as specified. DBond was used for identification of intra- and interprotein disulfide-linked peptides from MS/MS spectra. Only significant hits ($p < 0.05$ by Mascot probability analysis) were accepted. The Mascot score threshold was set as a 1% peptide-level FDR for confident peptide and protein identification.

Post-translational Modification Analysis

The raw data files obtained from the MS were converted to mascot generic files using Mascot Daemon (version 2.8.0). Database searching was performed using Mascot Server (version 2.4.2, https://www.matrixscience.com/daemon.html) against the SwissProt human database (version 57.15, 20,233 entries). Searches were conducted with trypsin digestion allowing up to one missed cleavage and the standard variable modifications listed below: acetylation (K), dehydroalanine (C), deamidation (NQ), glygly (K), oxidation (M), phosphorylation (ST and Y), propionamide (C), and trioxidation (C). Post-translational modifications (PTMs) were initially identified using these settings. PTM-containing peptides identified from individual gel bands were subsequently combined into a single integrated dataset for downstream analysis.

To further evaluate the influence of TMT labeling on PTM assignment, two additional Mascot searches were performed in which TMT was specified either as a fixed or a variable modification at the peptide N-terminus and lysine residues. For all PTM-containing peptides listed in Supplemental Table S2, stringent filtering criteria were applied (Δ mass $\leq$0.1 Da, Mascot score $\geq$30, and E-value <0.05). Also, peptides containing only propionamide-modified Cys residues were excluded from the final dataset. These thresholds were uniformly applied across all search configurations.

Disulfide-linked peptides were identified using DBond (http://prix.hanyang.ac.kr/), a specialized algorithm for detecting disulfide-linked peptides pairs. Searches were restricted to Mascot-identified proteins, and only high-confidence results (DBond score $\geq$3.5 and both linked peptides $\geq$6 amino acids) were retained, and all assignments were verified through automatic and manual spectral interpretation.

Protein Interference and Isoform Assignment

Protein identifications were derived from peptide-level evidence, with accession numbers provided for all detected proteins. Isoform specificity was assessed by the presence of unique peptides using the neXtProt Peptide Uniqueness Checker (http://nextprot.cn/tools/peptide-uniqueness-checker), and interprotein disulfide bonds were further validated using DBond to distinguish isoform-dependent linkages.

Puromycin Assay

MDA-MB-231 cells were seeded in 60 mm cell culture dishes at a density of 6.0 x 10^5 cells. After 24 h, cells were treated with H_2O_2 (0.1, 0.25, 0.5, or 1 mM) in PBS for 1 h. The buffer was then replaced with a fresh medium containing puromycin, and cells were incubated for 0.5, 2, 6, or 12 h to label nascent peptides. The cells were then incubated with 1 μg/ml of puromycin in the medium for 1 h before harvest. The samples were lysed, and puromycin-incorporated nascent peptides were detected using a puromycin antibody (Millipore).

Endogenous Immunoprecipitation in Non-reducing Condition

MDA-MB-231 cells (2.2 x 10^6 cells) were seeded in 100 mm cell culture dishes and harvested 24 h later. Subsequently, the cells were lysed using RIPA buffer, and the lysate concentration was determined via BCA assay. 500 μg of lysates were used for endogenous immunoprecipitation. The lysates were incubated overnight at 4 °C with 10 μg of normal rabbit IgG (Cell signaling 2729) as a control or γ-actin rabbit monoclonal antibody (Abcam, ab200046) to detect endogenous actin. Protein G Sepharose 4 Fast Flow (Cytiva, 17–0618–01) 40 μl were added to each solution and incubated for an additional 3 h at 4 °C. The lysates were then centrifuged to precipitate beads, washed 3 times, and boiled for 5 min at 95 °C in a non-reducing sample buffer. The samples were separated and silver stained, as mentioned above.

Experimental Design and Statistical Rationale

Statistical analyses were performed using one-way ANOVA followed by Tukey's post hoc test and two-tailed unpaired Student's *t*-tests for comparisons with control. The choice of tests was based on the approximate normality of replicate distributions, verified by inspection of residuals. A p-value <0.05 was considered significant.

Quantification and Reliability

Reporter ion–based quantification (TMT) was performed across all fractions. Normalization of peptide abundances was carried out relative to the 0 mM H_2O_2 condition. To assess TMT labeling efficiency, an additional Mascot search was performed in which TMT (6-plex) was defined as a variable modification at the peptide N-terminus and lysine residues. Among all PTM-containing peptides identified under this configuration, over 99.9% were labeled with TMT, confirming highly efficient and consistent TMT tagging.

Data Analysis

Pathway analysis, enrichment analysis, and principal component analysis were performed using MetaboAnalyst 6.0 (https://www.metaboanalyst.ca/) on metabolites exhibiting over 20% variation after treatment with 1 mM H_2O_2 compared to that at 0 mM H_2O_2. Metabolite graphs were generated using GraphPad Prism 9. Protein–protein interaction networks and protein classifications were analyzed using STRING (STRING version 12.0, https://string-db.org/) and PANTHER (https://www.pantherdb.org/). Graphic comparisons of sensitive and insensitive protein subgroups according to PANTHER classification were performed using the graphing functions of SRplot (https://www.bioinformatics.com.cn/srplot). Intra-disulfide or Inter-disulfide bonds were identified using the DBond program from PRIX (https://prix.hanyang.ac.kr/download/dbond.jsp) and visualized using Cytoscape (20).

RESULTS

To assess cellular responses to varying oxidative stress levels, we performed metabolomic and proteomic analyses on cells treated with 0.1 to 1 mM H_2O_2 (Fig. 1), using standard workflows for each omics platform.

Redox-Sensitive Pathways Identified by Metabolomics in Oxidative Stress

To assess concentration-dependent metabolic responses to oxidative stress, we performed LC-MS–based metabolomics on MDA-MB-231 cells treated with 0 to 1 mM H_2O_2 for 1 h. Metabolites were extracted using cold methanol–water–chloroform (3:2:2) and analyzed by HPLC-MS, with five replicates per condition. A total of 79 intracellular metabolites were quantified. Heatmap and principal component analysis analysis confirmed clear separation of samples based on H_2O_2 concentration (Fig. 2, *A–B*).

Metabolites were classified into three groups. Group I (e.g., 6-phosphogluconate, ADP, UDP, pyruvate) showed a transient increase at 0.1 mM, followed by decline. Group II (e.g., AICAR (5-Aminoimidazole-4-carboxyamide ribonucleoside), SAICAR (succinyl-AICAR), ATP, GTP, phosphoribosyl pyrophosphate (PRPP) decreased progressively. Group III (58 metabolites) increased dose-dependently. Pathway analysis of >20% changing metabolites at 1 mM H_2O_2 revealed oxidative sensitivity in purine/pyrimidine metabolism, the pentose phosphate pathway (PPP), the tricarboxylic acid (TCA) cycle, glycolysis/gluconeogenesis, and amino acid metabolism (Fig. 2*C*, Supplemental Fig. S1).

Glycolysis showed early metabolite accumulation (G6P, DHAP) with downstream depletion, suggesting redox-sensitive blockades (Supplemental Fig. S2*A*). In the TCA cycle, citrate and succinate increased, while malate decreased, implying disrupted flux due to altered NAD^+/FAD (Supplemental Fig. S2*B*). The PPP showed enhanced NADPH production but GSSG accumulation, suggesting NADPH depletion (Supplemental Fig. S2, *C–D*). Nucleotide pathways showed precursor depletion and imbalance (Supplemental Fig. S2, *E–F*), and many amino acids peaked at moderate ROS, reflecting inhibited translation (Supplemental Fig. S2*G*). These changes reflect targeted metabolic rewiring under oxidative stress.

Proteomic Analysis of Protein Diversity under Non-reducing Conditions

Since cellular metabolites and pathways responded differently to oxidative stress, we examined redox-sensitive proteomic changes under non-reducing conditions across varying H_2O_2 concentrations (0–1 mM). MDA-MB-231 cells

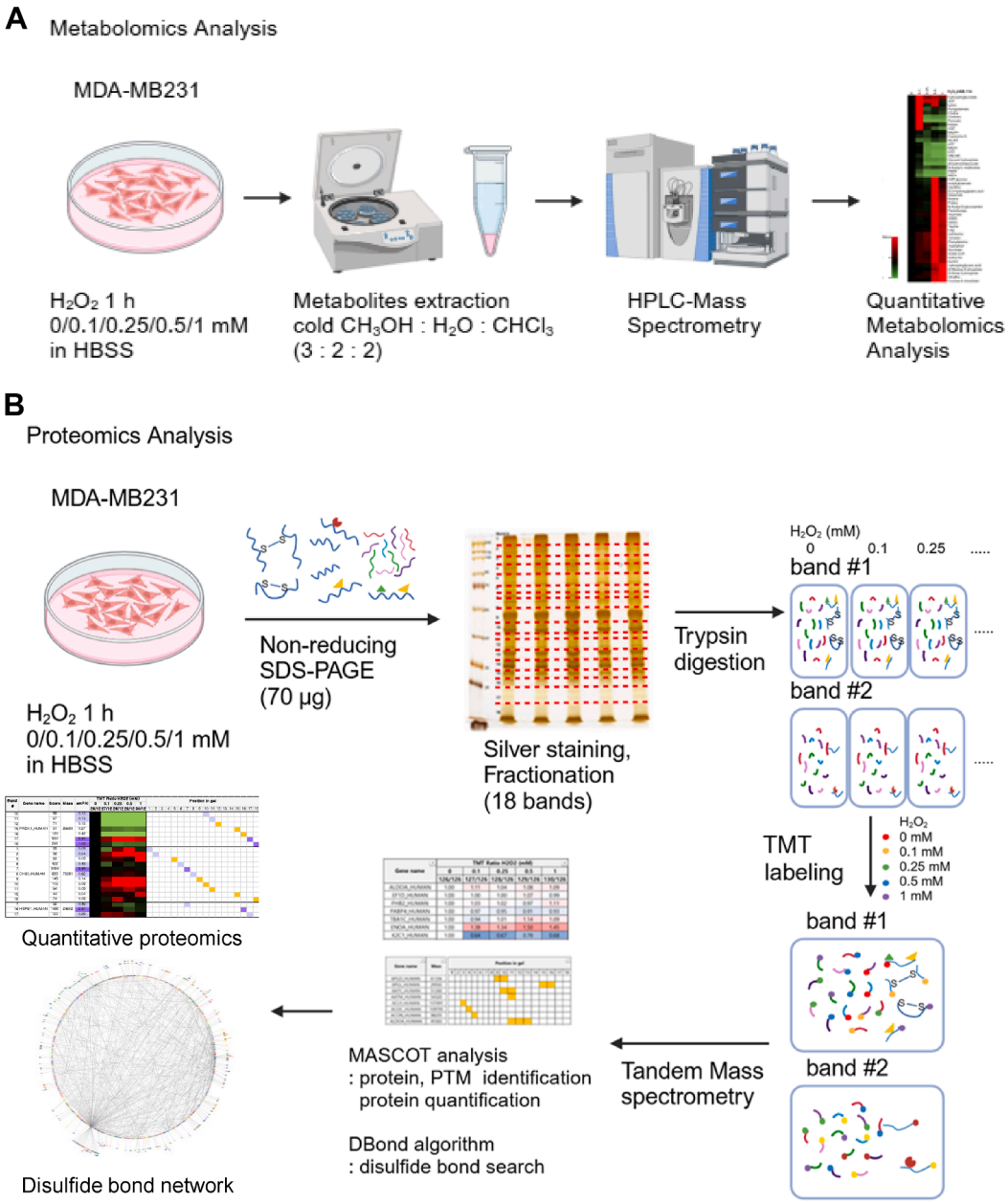

FIG. 1. **Schematic overview of the metabolomics and proteomics workflow MDA-MB-231 cells was treated with various concentrations of H_2O_2 before processing for proteomics and metabolomics analyses**. *A*, metabolomics workflow. Following H_2O_2 treatment, hydrophilic metabolites were extracted, before being analyzed using HPLC-MS. *B*, proteomics workflow. Cell lysates were prepared in a non-reducing sample buffer following H_2O_2 exposure. Different TMT reagents were used to label samples corresponding to each H_2O_2 concentration.

were treated for 1 h, and proteins were separated by non-reducing PAGE, followed by silver staining (Fig. 1, Supplemental Fig. S3). Gels were divided into 18 bands, digested, labeled with 6 TMT tags, and quantified via mass spectrometry. Proteins were filtered based on peptide scores (≥20), ≥2 unique peptides, and standard deviations (≤1.3). PTMs were identified using MASCOT (12). A total of 1669 protein bands corresponding to 1062 proteins were quantified, including information on band positions, exponentially modified Protein Abundance Index (emPAI), TMT ratios and PTMs.

Among the identified proteins, 14 appeared across ≥9 bands and 83 across 3 to 8 bands (Supplemental Fig. S4). These proteins included PRDX1, which formed high-molecular-weight oligomers under oxidative stress (21), and proteins with distributed emPAI values such as keratins, and GAPDH with one dominating emPAI values (22).

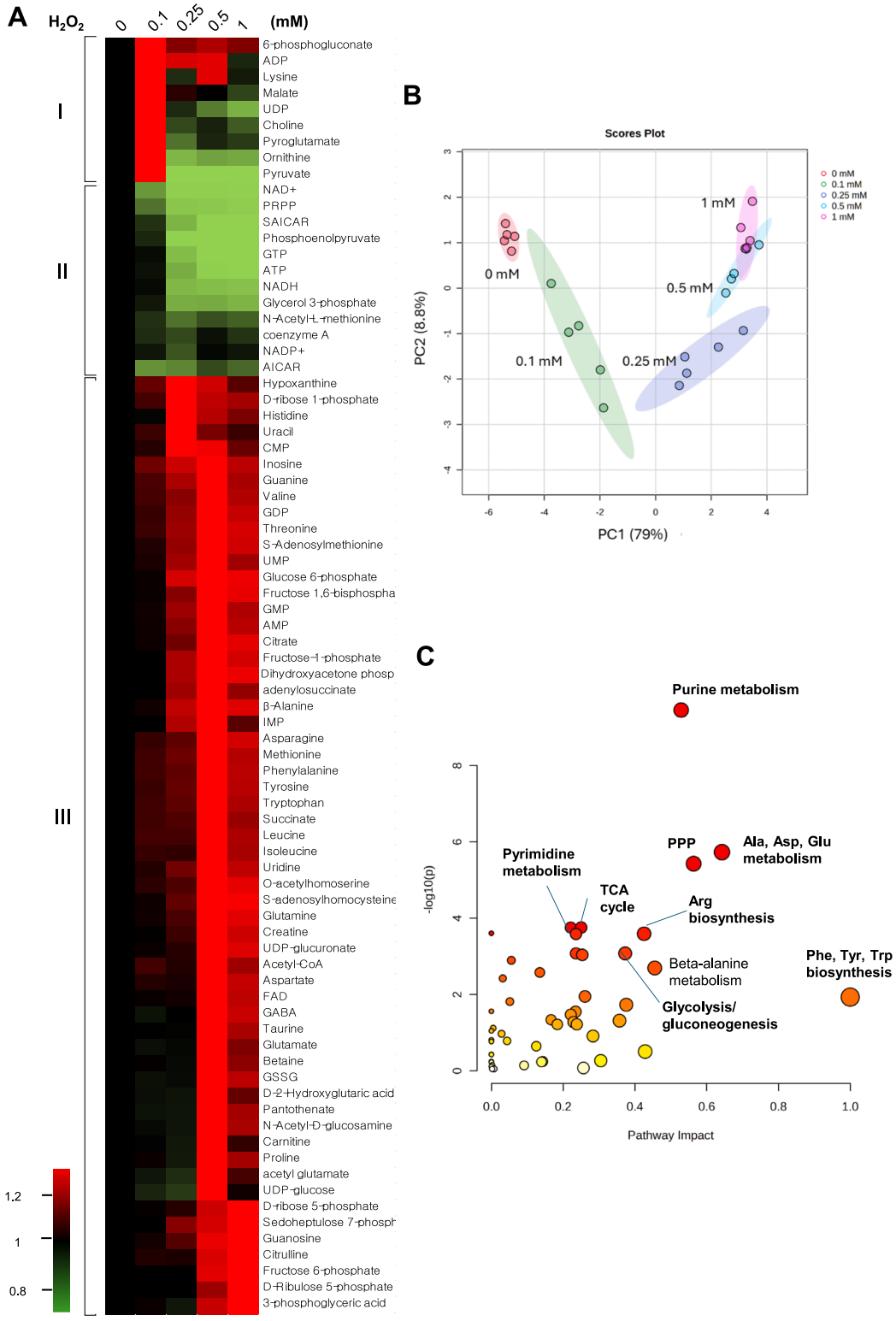

FIG. 2. **Metabolite changes under oxidative stress conditions**. *A*, heatmap showing metabolite changes across H_2O_2 concentrations. Metabolites were categorized into three groups based on their response patterns. *B*, Principal component analysis of metabolite profiles for H_2O_2 concentration. *C*, pathway analysis of redox-sensitive metabolic pathways using MetaboAnalyst 6.0. Only metabolites exhibiting >20% change at 1 mM H_2O_2 were included. Supplemental Fig. S1*B* illustrates detailed values and the full list of affected pathways.

Cytoskeletal proteins displayed various quantitative changes across multiple bands. Unlike GAPDH, which concentrated in a single main band, cytoskeletal proteins (*e.g.*, K2C1, K1C9) were evenly distributed with maximum emPAI (~1.1), showing broad band patterns with distinct TMT shifts (Supplemental Fig. S5). These results suggest keratins exist in multiple stable forms.

To validate the MS findings, Western blotting was conducted for six proteins (Fig. 3). Each showed multiple bands under non-reducing conditions, with primary bands being relatively unresponsive and secondary bands highly sensitive to H_2O_2. These secondary bands were often detected only in MS due to low abundance (emPAI <1% of the primary) and required higher lysate input for Western detection. PRDX1 upper bands decreased ~70% at 0.5 mM H_2O_2, while the main band increased 1.5-fold at 0.25 mM. Western confirmed PRDX1 dimers, which diminished as H_2O_2 increased, supporting disulfide-dependent regulation.

Similarly, heat shock protein 60 (HSP60/CH60) showed ≥1.4-fold increases in upper bands at ≥0.25 mM H_2O_2, with minimal change in the dominant band. Detection of secondary bands required increased lysate loading. Heat shock protein beta-1 (HSP27/HSPB1) upper bands decreased (0.81–0.87-fold) at 0.5 mM, while primary bands were largely unchanged. GAPDH upper bands increased up to 1.4-fold at 1 mM H_2O_2 but were undetectable by Western due to the large emPAI value of primary band (332.13). Heat shock protein 90 beta (HS90 B) lower bands increased 1.7-fold at 0.25 mM but were detected regardless of redox conditions, suggesting a disulfide-independent mechanism. Enolase-1 (ENOA) showed up to 1.5-fold increases in secondary bands at 0.5 mM H_2O_2, consistent with disulfide-dependent Western results.

In conclusion, MS provided higher sensitivity than Western for detecting redox-induced changes in low-abundance protein subpopulations. The redox-responsive secondary bands, often invisible in Western blotting, suggest that minor protein populations undergo disulfide-mediated regulation under oxidative stress.

Secondary Protein Bands Reflect Oxidative Stress–Induced Post-translational Modifications

Multiple secondary bands and their redox-responsive changes were commonly observed across proteins. We analyzed PTMs of these secondary proteins using MASCOT-based MS/MS spectra identification. A detailed proteomic comparison between primary and secondary bands was conducted to assess PTM patterns and redox-induced abundance shifts. PTMs included ubiquitination (GlyGly) and acetylation on Lys, phosphorylation on Ser/Thr/Tyr, deamidation on Asn/Gln, oxidation on Met, and several Cys modifications such as propionamide adducts, dehydroalanine, and trioxidation—indicative of irreversible oxidation (11, 12).

Although numerous PTM candidates were initially detected in secondary bands, these bands generally exhibited markedly lower protein abundance (low emPAI values), resulting in weaker MS/MS fragmentation (22). After applying stringent filtering thresholds (Δ mass <0.1 Da, Mascot score ≥30, E-value ≤0.05) and excluding peptides containing only propionamide-modified Cys residues (considered processing-derived artifacts), 521 peptides from 131 proteins remained as confidently identified PTMs (Supplemental Table S2, Supplemental Fig. S7).

For most proteins (*e.g.,* HS90 A/B and GAPDH), high-confidence PTMs were detected primarily in the major band, where the emPAI value was up to several hundred-fold higher than in secondary bands (Supplemental Fig. S6, *A–B*). For example, GAPDH showed quantifiable abundance changes across 10 secondary bands under oxidative stress; however, its major band at ~36 kDa (band 13) exhibited an extremely large emPAI value of 332.13, which was >114-fold higher than that of any secondary band, and this band retained most of confidently identified PTMs after stringent filtering. Similarly, the metabolic enzyme triosephosphate isomerase displayed quantification in three bands, but its major band (band 16; emPAI = 49.49), showing a >48-fold higher abundance than the others, was the only band in which high-confidence PTMs were detected.

However, several proteins retained confidently identified PTMs across relatively abundant secondary bands even after strict filtering (Supplemental Fig. S6, *C–D*). For example, actin isoforms showed comparable emPAI values across bands 10 to 12 (e.g., 6.78/5.34/5.34 for ACTA and 30.30/24.46/17.04 for ACTB), and identical modified peptide sequences were detected in all three bands. Likewise, pyruvate kinase isozyme M1/M2 (KPYM) exhibited similar abundance in bands seven and eight (emPAI = 11.83 and 13.13), enabling confident detection of the same PTM at both positions. These observations suggest that only higher-abundance secondary bands retain confidently identifiable PTMs under our experimental and filtering conditions.

TMT-Based Classification of Redox-Sensitive Protein Isoforms

To classify redox-sensitive proteins, we analyzed TMT ratio changes across 1669 bands from 1062 proteins using nanoLC-MS/MS, with 0 mM H_2O_2 as the control. Proteins were grouped based on the band showing the most significant TMT ratio change (≤0.875 or ≥1.25) at the lowest H_2O_2 concentration (Fig. 4*A*). Group I (180 proteins), including PRDX1 and HSP60, responded at 0.1 mM H_2O_2; Group II (80), including GAPDH and PPIA, at 0.25 mM; Group III (88), including ROA2, at 0.5 mM; Group IV (86), including 14-3-3 beta/alpha, at 1 mM. Group V (628 proteins), including PDIA6 and ARPC3, showed no change across all conditions (Supplemental Table S3).

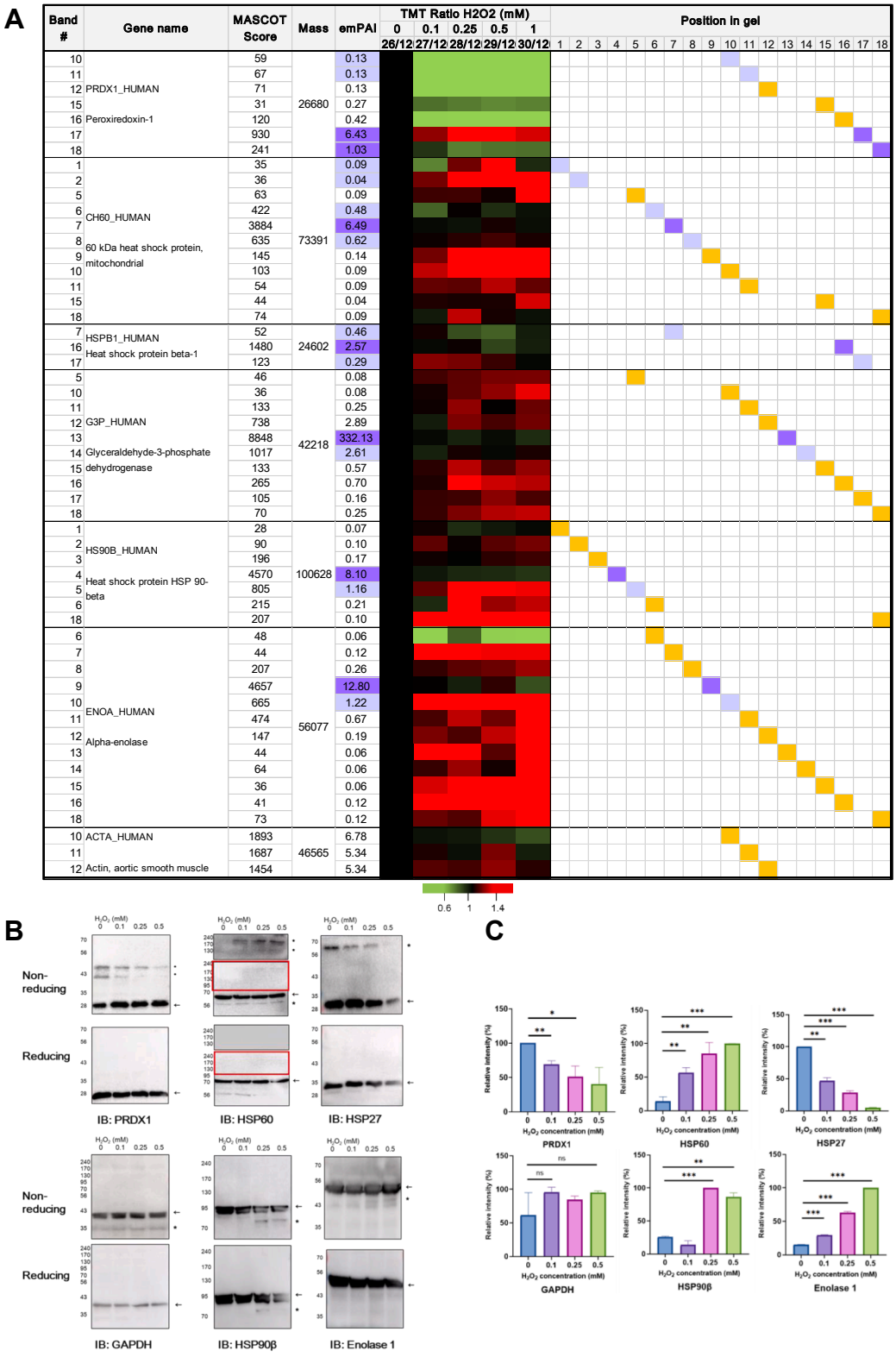

FIG. 3. **Western blot validation of mass spectrometry results**. Selection of proteins with significant abundance changes for validation. *A*, TMT ratios ≤0.6 are shown in *green*, and ratios ≥1.4 are shown in *red*. Main Western blot bands are marked in *purple* and secondary bands in pale purple. ACTA_HUMAN serves as the negative control. *B*, Western blot analysis of proteins in panel *A* under non-reducing and reducing conditions. Equal amounts of lysate and identical exposure times were maintained. *Arrows* indicate main bands (*purple*), and asterisks indicate

We further analyzed the 434 redox-sensitive proteins (Groups I–IV) using STRING (v12.0; http://string-db.org/) and PANTHER classifications (Fig. 4*B*). These proteins spanned diverse classes, including chaperones, cytoskeletal proteins, chromatin regulators, RNA/DNA metabolism proteins, translation-related proteins, modifying enzymes, transporters, and adaptors. In contrast, redox-insensitive proteins in Group V showed no significant class distribution differences (data not shown). Notably, even within the same complexes, such as ribosomes, individual proteins exhibited distinct TMT ratio changes (Supplemental Fig. S8), reflecting heterogeneous redox responses.

Functional enrichment analysis using STRING revealed that redox-sensitive proteins were predominantly involved in RNA metabolism, translation, protein folding, localization, and metabolism (Fig. 4*C*). These processes likely reflect rapid responses to oxidative damage, facilitating turnover and repair. In contrast, redox-insensitive proteins were primarily associated with general metabolic functions. This discrepancy suggests that oxidative stress triggers coordinated changes in redox-sensitive pathways, while metabolic responses are limited to specific enzymes, as also indicated by our metabolomics data. Although metabolism-related pathways were enriched among the insensitive group, key enzymes like PRDX1, GAPDH, and enolase exhibited diverse TMT ratio shifts and PTMs across secondary bands (Fig. 3*A*), indicating selective regulation by redox state.

Redox-Sensitive Enzyme Modulation Disrupts Metabolic Pathways under Oxidative Stress

To validate the effects of oxidative stress on cellular metabolism, we integrated proteomic data on redox-sensitive enzymes with metabolic pathway maps (Supplemental Fig. S9, Supplemental Table S4). We focused on metabolic enzymes located at pathway reflux positions (Supplemental Fig. S2).

Previously, we observed a reversed ratio of glyceraldehyde 3-phosphate and 3-phosphoglycerate under oxidative stress (Supplemental Fig. S2*A*), implicating dysfunction of GAPDH and phosphoglycerate kinase 1. Although both act sequentially in glycolysis, their proteomic responses differed. phosphoglycerate kinase 1 showed minimal changes, while GAPDH appeared in 10 bands, with secondary bands increasing up to 1.5-fold. Other glycolytic enzymes (*e.g.,* PGAM, enolase, pyruvate kinase) also showed dynamic changes in TMT ratios (Supplemental Table S4).

TCA cycle enzymes responded variably. Succinate dehydrogenase (SDH) increased up to 1.3-fold and showed Cys oxidation. Malate dehydrogenase and citrate synthase also changed, corresponding to altered metabolite levels, such as citrate and succinate accumulation and malate and ATP depletion (Supplemental Fig. S2*B*). These changes suggest that oxidative stress disrupts TCA cycle flux via quantitative enzyme regulation.

The oxidative branch of the PPP, crucial for NADPH production, was disrupted, with enzymes like 6-phosphogluconolactonase and 6-phosphogluconate dehydrogenase showing significant TMT ratio changes. Despite stable NADPH levels, increased GSSG indicated insufficient reducing power (Supplemental Fig. S2*D*). The non-oxidative PPP enzymes, including transketolase and transaldolase (TAL), remained unchanged.

In nucleotide biosynthesis, PRPS1, involved in PRPP production, increased by >20% at 1 mM H_2O_2 and exhibited PTMs such as Cys oxidation and phosphorylation. ATIC showed a >20% reduction in upper band intensity under stress, indicating redox-modulated activity. Nucleoside diphosphate kinase-B remained stable, while NDPK-A is known to lose activity through oxidative dissociation (6, 7).

Most amino acids accumulated under oxidative stress, peaking at 0.5 mM H_2O_2. Histidine peaked earlier at 0.25 mM before declining; lysine remained unchanged. These patterns likely reflect translational inhibition, confirmed by puromycin incorporation assays showing dose-dependent repression (Supplemental Fig. S10), contributing to amino acid accumulation (Supplemental Fig. S2*G*).

Together, our findings highlight that oxidative stress alters metabolism through both quantitative changes in enzymes. GAPDH, SDH, and oxidative PPP enzymes emerge as central redox-sensitive regulators. For detailed data, see Supplemental Table S4 and Supplemental Figure S9.

Identification of Intra- and Inter-disulfide Crosslinked Proteins

To identify disulfide-bonded proteins and associated Cys residues, we analyzed MS/MS data from proteins prepared under non-reducing conditions (Fig. 1). Disulfide-linked peptides were detected using the DBond algorithm, which identifies crosslinked peptides based on fragmentation patterns (12). A total of 68,038 disulfide-linked peptides were identified, corresponding to 1287 unique protein pairs (Supplemental Table S5).

To ensure reliability, peptides with low DBond scores (<3.5), short sequences (<6 residues), or ambiguous origins were filtered using the neXtProt Peptide Uniqueness Checker (http://nextprot.cn/tools/peptide-uniqueness-checker), yielding 21,059 high-confidence disulfide bonds from 1185 proteins and 16,666 unique Cys site pairs. Representative MS/MS spectra of disulfide-linked peptides are shown in

secondary bands (*pale purple*) corresponding to each protein in panel *A*. *C*, quantification of Western blot bands shown in panel *B*. Band intensities were normalized to the 0 mM H_2O_2 condition for each protein and plotted as relative intensity (%). Data represent mean ± standard deviation (n = 3). *$p < 0.05$; **$p < 0.01$; ***$p < 0.001$; ns = not significant.

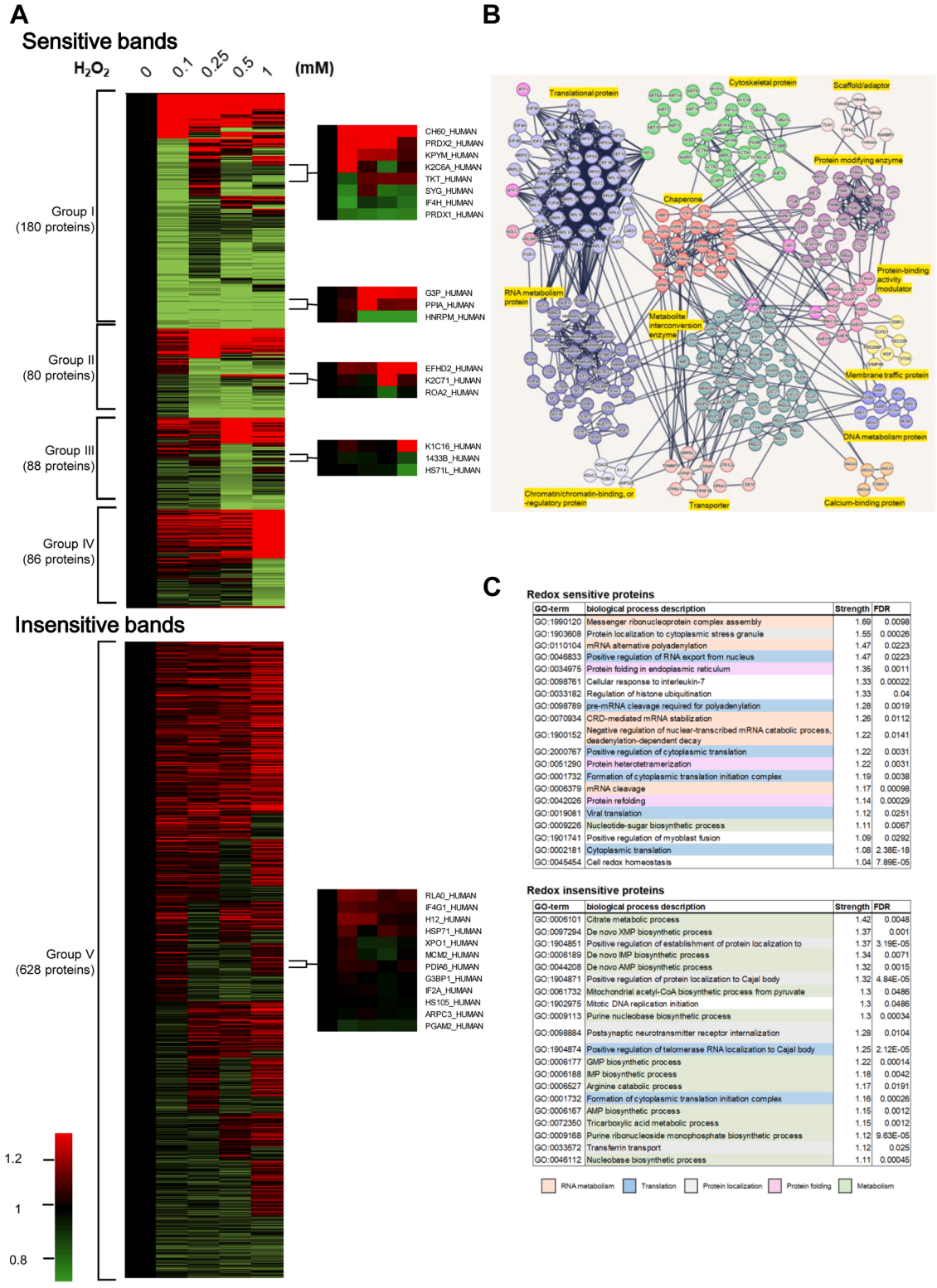

Redox sensitive proteins

GO-term	biological process description	Strength	FDR
GO:1990120	Messenger ribonucleoprotein complex assembly	1.69	0.0098
GO:1903608	Protein localization to cytoplasmic stress granule	1.55	0.00026
GO:0110104	mRNA alternative polyadenylation	1.47	0.0223
GO:0046833	Positive regulation of RNA export from nucleus	1.47	0.0223
GO:0034975	Protein folding in endoplasmic reticulum	1.35	0.0011
GO:0098761	Cellular response to interleukin-7	1.33	0.00022
GO:0033182	Regulation of histone ubiquitination	1.33	0.04
GO:0098789	pre-mRNA cleavage required for polyadenylation	1.28	0.0019
GO:0070934	CRD-mediated mRNA stabilization	1.26	0.0112
GO:1900152	Negative regulation of nuclear-transcribed mRNA catabolic process, deadenylation-dependent decay	1.22	0.0141
GO:2000767	Positive regulation of cytoplasmic translation	1.22	0.0031
GO:0051290	Protein heterotetramerization	1.22	0.0031
GO:0001732	Formation of cytoplasmic translation initiation complex	1.19	0.0038
GO:0006379	mRNA cleavage	1.17	0.00098
GO:0042026	Protein refolding	1.14	0.00029
GO:0019081	Viral translation	1.12	0.0251
GO:0009226	Nucleotide-sugar biosynthetic process	1.11	0.0067
GO:1901741	Positive regulation of myoblast fusion	1.09	0.0292
GO:0002181	Cytoplasmic translation	1.08	2.38E-18
GO:0045454	Cell redox homeostasis	1.04	7.89E-05

Redox insensitive proteins

GO-term	biological process description	Strength	FDR
GO:0006101	Citrate metabolic process	1.42	0.0048
GO:0097294	De novo XMP biosynthetic process	1.37	0.001
GO:1904851	Positive regulation of establishment of protein localization to	1.37	3.19E-05
GO:0006189	De novo IMP biosynthetic process	1.34	0.0071
GO:0044208	De novo AMP biosynthetic process	1.32	0.0015
GO:1904871	Positive regulation of protein localization to Cajal body	1.32	4.84E-05
GO:0061732	Mitochondrial acetyl-CoA biosynthetic process from pyruvate	1.3	0.0486
GO:1902975	Mitotic DNA replication initiation	1.3	0.0486
GO:0009113	Purine nucleobase biosynthetic process	1.3	0.00034
GO:0098884	Postsynaptic neurotransmitter receptor internalization	1.28	0.0104
GO:1904874	Positive regulation of telomerase RNA localization to Cajal body	1.25	2.12E-05
GO:0006177	GMP biosynthetic process	1.22	0.00014
GO:0006188	IMP biosynthetic process	1.18	0.0042
GO:0006527	Arginine catabolic process	1.17	0.0191
GO:0001732	Formation of cytoplasmic translation initiation complex	1.16	0.00026
GO:0006167	AMP biosynthetic process	1.15	0.0012
GO:0072350	Tricarboxylic acid metabolic process	1.15	0.0012
GO:0009168	Purine ribonucleoside monophosphate biosynthetic process	1.12	9.63E-05
GO:0033572	Transferrin transport	1.12	0.025
GO:0046112	Nucleobase biosynthetic process	1.11	0.00045

FIG. 4. **Classification and network analysis of redox-sensitive proteins**. *A*, heatmap of redox-sensitive and redox-insensitive proteins. Proteins were classified into five groups based on the concentration at which the band intensity changed by ≤ 0.875 or ≥ 1.25. TMT ratios ≤ 0.8 are shown in *green* and ≥ 1.2 in *red*. Supplemental Table S3 presents detailed TMT ratio values and group assignments. *B*, STRING network of 434 proteins with TMT ratios ≤ 0.875 or ≥ 1.25 at any H_2O_2 concentration. Proteins within the same PANTHER protein class were clustered and color-coded accordingly. Edge thickness indicates the confidence level of predicted protein–protein interactions; only interactions with the

Supplemental Figure S11. Actin, for example, formed high-confidence disulfide crosslinks with multiple proteins such as pyruvate kinase and vimentin, which were validated by immunoprecipitation under non-reducing conditions (Supplemental Fig. S12).

Among these, 3483 disulfide crosslinks (involving 2856 site pairs across 1006 proteins) were associated with shifts to higher molecular weight bands than their canonical counterparts, suggesting that inter-disulfide bonding alters electrophoretic mobility under non-reducing conditions. These results provide a large-scale, previously underappreciated dataset of disulfide-linked proteins and their reactive Cys residues.

To explore the redox-regulated interaction network, a disulfide bond network was constructed using Cytoscape (v3.10.3; https://cytoscape.org) (20) (Fig. 5*A*). Only protein-specific peptides and bonds supported by at least three linkages per protein pair were included. The resulting network included 5275 disulfide bonds connecting 1064 protein pairs among 637 proteins. Louvain clustering via ClusterMaker2 revealed modular subclusters based on connection density (Fig. 5, *B–C*, Supplemental Fig. S13). Some subclusters (Fig. 5*B*) showed gene ontology (GO) enrichment, suggesting functional relatedness, while others (Fig. 5*C*) lacked significant GO terms, indicating novel or uncharacterized redox-regulated protein groups.

Overall, this analysis identified over 21,000 high-confidence disulfide bonds in more than 1100 proteins. The disulfide network illustrates widespread and functionally diverse redox-driven interactions that have been largely missed under conventional reducing conditions, underscoring the structural and regulatory roles of disulfide bonding under oxidative stress.

Specificity of disulfide Bindings Between Proteins

To evaluate whether disulfide bond formation is specific, we analyzed structural and sequence features surrounding Cys residues using our high-confidence disulfide bond dataset.

Among 15,752 Cys residues in 1163 proteins with DBond scores ≥3.5, only 32.7% (5137) participated in disulfide bonding (Fig. 6*A*, Supplemental Table S6). This selective pattern was consistent across protein sizes. For example, proteins with ≤5 Cys residues often showed >50% disulfide usage, whereas in proteins with >50 Cys residues, only 3.0% reached this threshold, indicating that disulfide bond formation is not proportional to Cys content or protein size (Fig. 6*B*). Even large proteins like titin (TITIN), SCO-spondin (SSPO), and stabilin-2 contained many Cys residues, yet only a small subset formed disulfide bonds. Similarly, large proteins with few disulfide-linked Cys residues, such as UBR4 and DNHD1, supported this selectivity.

To assess functional specificity, we focused on four large proteins (TITIN, SSPO, OBSCN, LRP1B), each with >50 disulfide-linked Cys residues. Among 726 interacting proteins with ≥3 DBond-supported links, distinct disulfide bonding partners were observed for each, indicating selective network integration (Fig. 6*C*).

Notably, disulfide crosslinks also varied across closely related isoforms. Using only high-confidence interactions (DBond score ≥3.5), we found that isoforms with highly conserved sequences often exhibited unique disulfide-linked partners (Fig. 7, Supplemental Fig. S14). For instance, the 14-3-3 isoforms (ε, σ, θ, ζ) shared overall structure and sequence, yet formed isoform-specific disulfide bonds. While both 14-3-3θ and ζ shared Cys25, 14-3-3θ crosslinked with DIAP1, whereas 14-3-3ζ interacted with α-aldolase, integrin β2, and TNFα-induced protein 8. The σ isoform used its unique Cys38 to link with Rab-5A and ESYT2, while Cys94 was primarily reactive in 14-3-3ζ (Fig. 7*A*), highlighting distinct redox networks despite structural similarity.

Another example is alpha-actinin (ACTN), an actin cross-linking protein. Although ACTN1 and ACTN4 share 86% sequence identity and eight conserved Cys residues, only ACTN1-specific residues (Cys180 and Cys370) formed disulfide bonds with 11 unique proteins, including pericentrin (Fig. 7*B*). This suggests disulfide bonds contribute to isoform-specific interaction profiles.

Enolase isoforms showed similar divergence. Enolase-γ, with a lower emPAI value (0.71), formed five or more disulfide bonds with choline-phosphate cytidylyltransferase A, a pattern not seen in the more abundant α (emPAI 12.80) or β (1.24) isoforms (Supplemental Fig. S14*D*). Similarly, Rab GDP dissociation inhibitor isoforms formed Cys302-dependent crosslinks with distinct RNA-binding proteins, including heterogeneous nuclear ribonucleoprotein L (Supplemental Fig. S14*G*).

Importantly, these isoform-specific disulfide networks did not correlate with protein abundance (Supplemental Table S1). For example, ACTN1/4 (1.51/1.90), ADT2/3 (0.39/0.28), and enolase γ (0.71) formed distinct disulfide bonds despite abundance similarity, suggesting structural context rather than expression level drives bonding specificity.

Together, these results indicate that disulfide bond formation is a selective process. Specific Cys residues act as redox-sensitive interaction hubs, enabling isoform-specific and functionally distinct protein networks. These findings suggest that disulfide bonds extend beyond structural roles

highest confidence score (≥0.900) are shown. *C*, top 20 biological processes enriched in redox-sensitive and redox-insensitive proteins; based on STRING analysis. Related processes are color-coded: RNA metabolism (*orange*), protein localization (*gray*), translation (*blue*), protein folding (*purple*), and metabolism (*green*).

to actively modulate protein interaction specificity and contribute to the functional diversification of isoforms.

Characteristics of Cys Residues Forming Disulfide Crosslinks

To characterize the sequence and structural features of Cys residues involved in disulfide bond formation, we compared the local amino acid environments surrounding disulfide-forming and non-disulfide-forming Cys. To minimize artifacts from low-confidence interactions, we analyzed only those Cys involved in ≥3 disulfide bonds, identifying 2930 Cys residues across 976 proteins—18.6% of the 15,752 total Cys sites (Supplemental Table S6). The remaining 12,822 Cys residues, either uninvolved or engaged in only 1 to 2 disulfide linkages, served as the comparison group.

Two key patterns emerged. First, positively charged amino acids—Arg and Lys—were enriched within ±10 residues of disulfide-forming Cys (Fig. 8, *A–C*; Supplemental Fig. S15), particularly at the +1 and + 2 positions. Arg appeared at 12.6% and 10.8%, and Lys at ~8% in these positions—nearly double the frequencies near non-disulfide Cys (Arg: 4.1%; Lys: 4.6%). In contrast, histidine, glutamate, and aspartate showed minimal differences between the groups. A pattern search in >16,000 proteins (https://prix.hanyang.ac.kr/download/PatternMatchFrm.jsp) revealed 16,507 CK/R or C x K/R motifs across 1547 proteins. However, only 22% were associated with disulfide formation, while 3653 motifs from 937 proteins were identified in our dataset, suggesting selective involvement despite motif abundance.

This enrichment of positively charged residues likely facilitates electrostatic stabilization of the thiolate anion, shifting the thiol–thiolate equilibrium toward the more reactive thiolate state and enhancing redox sensitivity.

Second, neighboring Cys residues were underrepresented around disulfide-forming sites, especially at the +1 and + 2 positions, where Cys frequency ranged from 0% to 2.95%, compared to 2.35 to 6.30% near non-disulfide Cys (Fig. 8, *D–F*). Pattern searches revealed 6863 CC and 6765 C x C motifs in the PRIX database, yet none of the CC and only 12 C x C motifs (from 10 proteins) were associated with disulfide bonds in our dataset. This suggests that adjacent Cys are spatially excluded from disulfide-forming regions, potentially to reduce steric hindrance or oxidative competition.

Together, these results identify two key features promoting disulfide bond formation (1): electrostatic enrichment of Arg and Lys, especially at +1/+2 positions, and (2) exclusion of adjacent downstream Cys. These findings support a model in which disulfide formation is affected by local sequence context and constrained by structural and functional considerations. Rather than occurring randomly, disulfide bond formation appears guided by sequence-driven stabilization and spatial selectivity, contributing to the efficiency and specificity of redox-based protein regulation.

DISCUSSION

In this study, we used non-reducing proteomics to identify redox-sensitive proteins and disulfide-linked networks, revealing how oxidative stress selectively modifies protein subpopulations and shapes their functions. Even minor protein subpopulations exhibited significant oxidative modifications under stress, highlighting the selectivity and compartmentalization of redox regulation. The identification of intra- and inter-protein disulfide bonds across a broad range of proteins provides a comprehensive map of disulfide networks across thousands of proteins. As demonstrated by reactive thiol probes such as NPSB-1, only a subset of cysteine residues exhibits reactivity under oxidative conditions (13). Isoform-specific disulfide formation, despite high sequence similarity, illustrates that disulfide bonding is a highly selective process shaped by local structural and contextual factors. Sequence analysis showed a strong enrichment of positively charged Lys/Arg residues near disulfide-prone cysteines, particularly at the +1/+2 positions, suggesting local charge influences thiolate formation and disulfide bonding (23).

These proteomic results align with metabolic findings showing that oxidative stress disrupts central metabolism such as glycolysis and the TCA cycle (24). Increased H_2O_2 concentrations led to accumulation of upstream glycolytic intermediates and reduced downstream products, redirecting flux toward the oxidative PPP to generate NADPH (Supplemental Fig. S2) (25, 26). Corresponding PTMs were found in PPP enzymes like G6PD and 6-phosphogluconate dehydrogenase (27), while GAPDH and SDH were inactivated via Cys oxidation (28, 29). Additionally, NDPK-A, another redox-sensitive metabolic enzyme, shifted from an active hexamer to an inactive dimer in an oxidation-dependent manner (30, 31). These redox induced modifications reinforce the connection between redox-sensitive enzyme regulation and metabolic rewiring (26).

Though not directly detected, inverse abundance trends between uridine and uracil and between UMP and UDP suggest redox-related modulation of uridine phosphorylase and UMP kinase. The sharp decline in His may reflect reduced PRPP availability due to ATP depletion under oxidative stress (32). In contrast, Lys remained stable, likely due to redundancy in its biosynthetic pathways—via oxaloacetate/aspartate or α-ketoglutarate (32)—allowing compensation. Other amino acids with single biosynthetic routes were more vulnerable to redox stress. Arg, which is synthesized through the complex urea cycle, was undetected.

Disulfide bond formation was a predominant Cys-based PTM enriched under oxidative conditions. GAPDH, PRDX1, and HSP60 showed multiple non-reducing SDS-PAGE bands, confirmed by MS/MS to represent redox-dependent PTM variants. These species were often absent under reducing conditions, underscoring the need to maintain disulfide

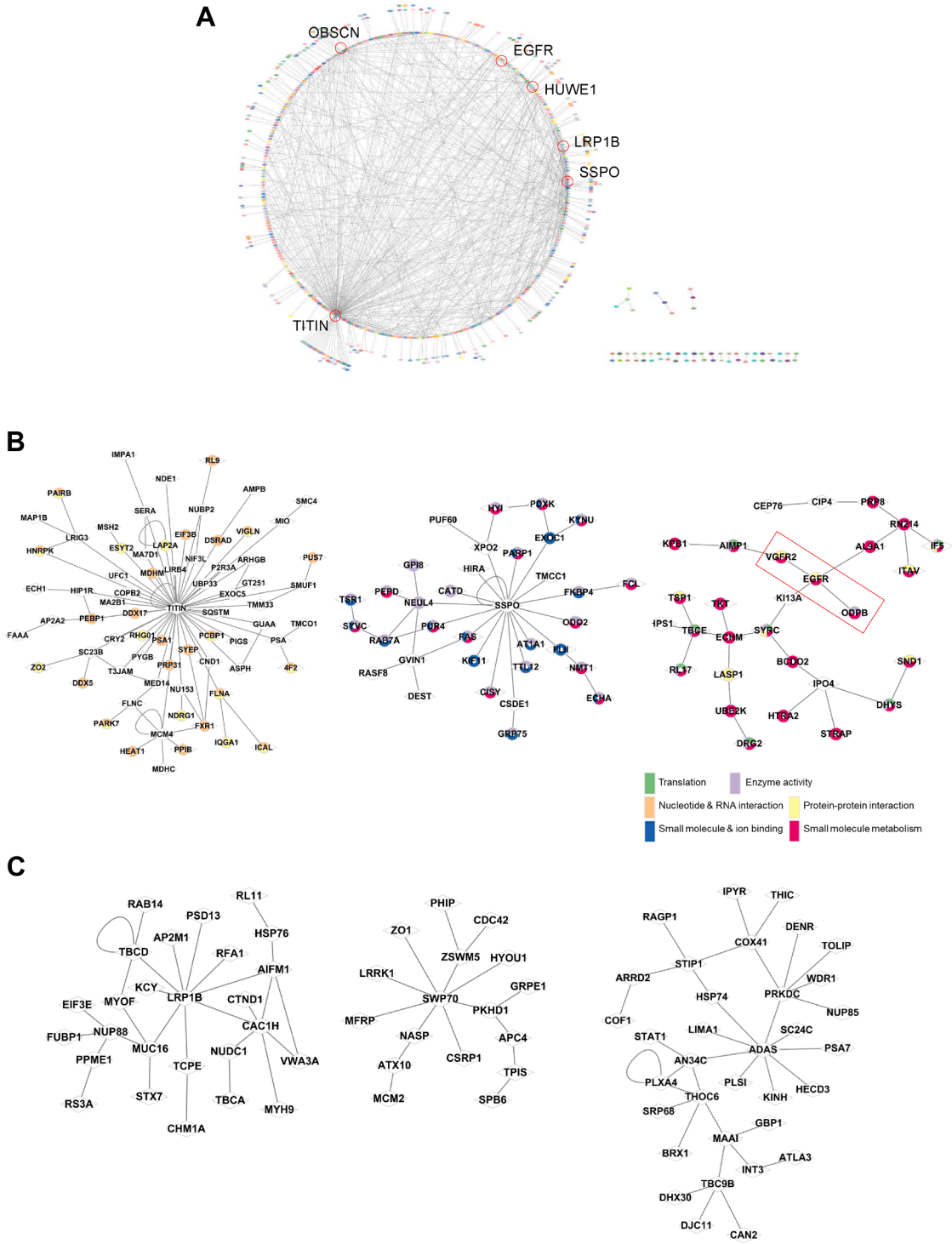

FIG. 5. **Disulfide bond network**. Global disulfide bond network among proteins. Disulfide linkages were identified using the DBond algorithm and visualized in Cytoscape. *A.* Only disulfide bonds observed in at least three independent peptides and not derived from isoform-conserved sequences were included. Each node represents a distinct protein, and each edge indicates recurring disulfide linkages observed three or more times. *B* and *C*, representative subclusters derived from multilevel clustering analysis. Subclusters containing proteins with known STRING interactions are shown in (*B*), while those without shared STRING interactions are shown in (*C*).

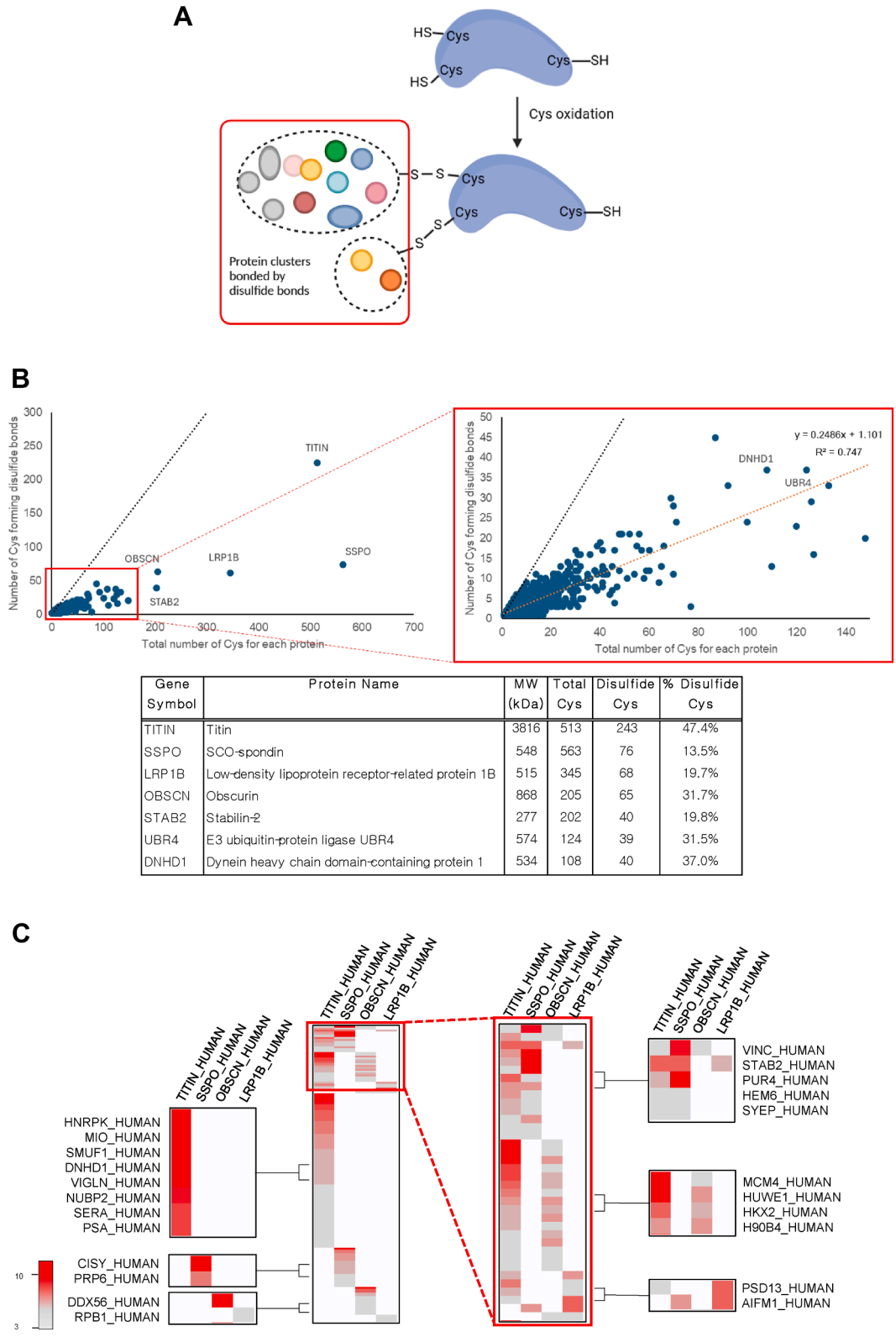

Gene Symbol	Protein Name	MW (kDa)	Total Cys	Disulfide Cys	% Disulfide Cys
TITIN	Titin	3816	513	243	47.4%
SSPO	SCO-spondin	548	563	76	13.5%
LRP1B	Low-density lipoprotein receptor-related protein 1B	515	345	68	19.7%
OBSCN	Obscurin	868	205	65	31.7%
STAB2	Stabilin-2	277	202	40	19.8%
UBR4	E3 ubiquitin-protein ligase UBR4	574	124	39	31.5%
DNHD1	Dynein heavy chain domain-containing protein 1	534	108	40	37.0%

FIG. 6. **Features of Cys residues in disulfide-bonded proteins**. *A*, schematic diagram showing subsets of Cys residues within individual proteins. Protein clusters sharing the same Cys binding sites were grouped using dotted lines. *B*, number of Cys residues forming disulfide bonds relative to the total number of Cys residues per protein. Protein names are indicated for those >200 total Cys residues. Supplemental Table S5 summarizes detailed values and protein names. *C*, heatmap showing proteins that interact with four large proteins (*e.g.,* TITIN, SCO-spondin, OBSCN, and LRP1B), each containing >50 disulfide-bonded Cys residues. To reduce non-specific interactions, only proteins with at least three recurrent binding events were included.

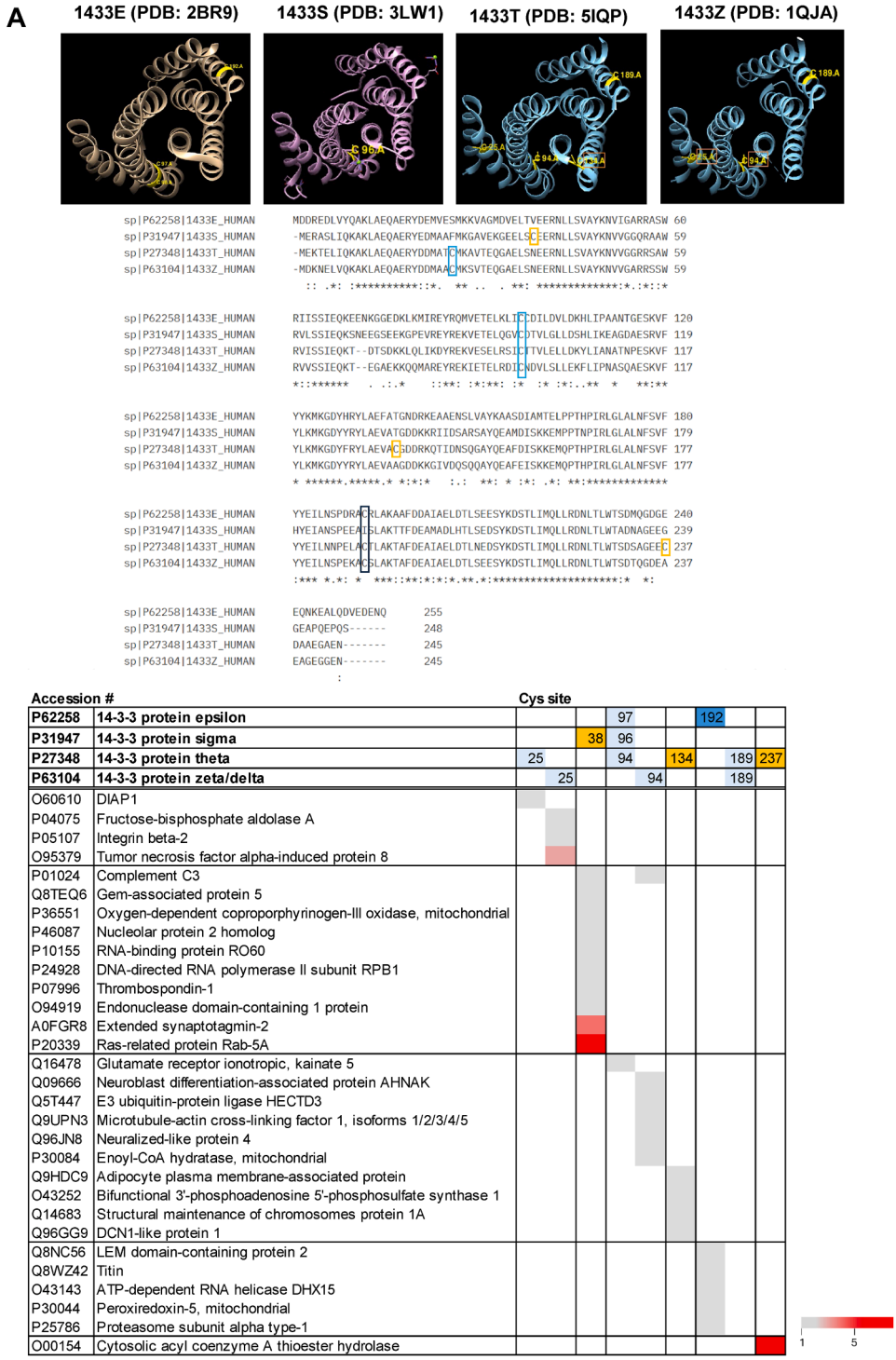

FIG. 7. **Homologous proteins with distinct disulfide bond clusters**. Disulfide-bonded protein groups were compared between isoforms with high-sequence homology and similar structural features. *A*, 14-3-3 proteins. *B*, alpha-actinin. Cys residues are shown in *yellow* on PDB or AlphaFold-predicted structures, with local sequence alignments provided. Binding partners for each Cys are listed in tables, with binding frequency color-coded: *gray* (1 detection) and red (≥5 detections). Only isoform-specific interactions with DBond scores ≥3.5 were included. In the alignments and tables, Cys residues were color-coded to reflect their distribution: isoform-specific Cys residues (*orange*); Cys residues shared by some isoforms (*light blue*); conserved Cys residues with biased disulfide linkage toward one isoform (*dark blue*). Supplemental Fig. S14 and Supplemental Table S5 depict additional examples.

B

Alpha-actinin-1 (AlphaFold: P12814)

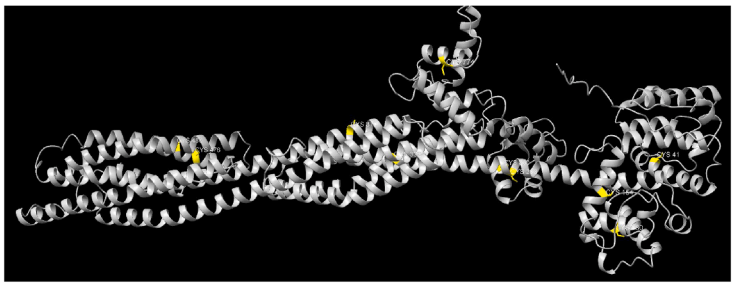

Alpha-actinin-4 (AlphaFold: O43707)

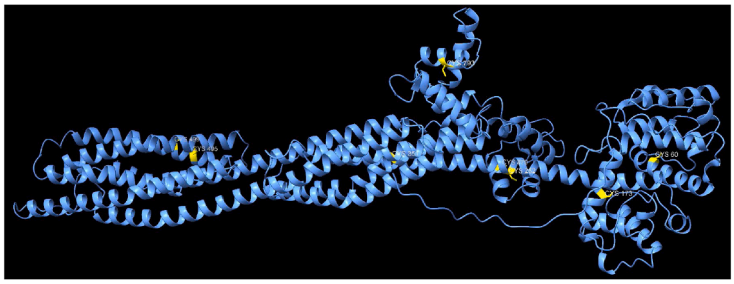

```
sp|P12814|ACTN1_HUMAN     KNVNIQNFHISWKDGLGFCALIHRHRPELIDYGKLRKDDPLTNLNTAFDVAEKYLDIPKM 221
sp|O43707|ACTN4_HUMAN     KNVNVQNFHISWKDGLAFNALIHRHRPELIEYDKLRKDDPVTNLNNAFEVAEKYLDIPKM 240
                          ****:***********.* ***********:*.*******:****.**:***********

sp|P12814|ACTN1_HUMAN     QTKLRLSNRPAFMPSEGRMVSDINNAWGCLEQVEKGYEEWLLNEIRRLERLDHLAEKFRQ 401
sp|O43707|ACTN4_HUMAN     QTKLRLSNRPAFMPSEGKMVSDINNGWQHLEQAEKGYEEWLLNEIRRLERLDHLAEKFRQ 420
                          *****************:*******.*  ***.**************************

sp|P12814|ACTN1_HUMAN     HSGTLGPEEFKACLISLGYDIGNDPQGEAEFARIMSIVDPNRLGVVTFQAFIDFMSRETA 821
sp|O43707|ACTN4_HUMAN     HGGALGPEEFKACLISLGYDVENDRQGEAEFNRIMSLVDPNHSGLVTFQAFIDFMSRETT 840
                          *.*:*****************: ** ****** ****:****: *:***************:
```

Accession #		Cys site			
P12814	**Alpha-actinin-1**	180	370	774	
O43707	**Alpha-actinin-4**				793
Q16658	Fascin				
P35579	Myosin-9				
O95613	Pericentrin				
P53618	Coatomer subunit beta				
Q5T447	E3 ubiquitin-protein ligase HECTD3				
O75369	Filamin-B				
Q96JN8	Neuralized-like protein 4				
Q9BW27	Nuclear pore complex protein Nup85				
Q8IY17	Patatin-like phospholipase domain-containing protein 6				
P46060	Ran GTPase-activating protein 1				
Q9UPZ6	Thrombospondin type-1 domain-containing protein 7A				
Q7L014	Probable ATP-dependent RNA helicase DDX46				
P45974	Ubiquitin carboxyl-terminal hydrolase 5				

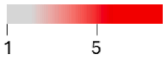

FIG. 7. *continued*

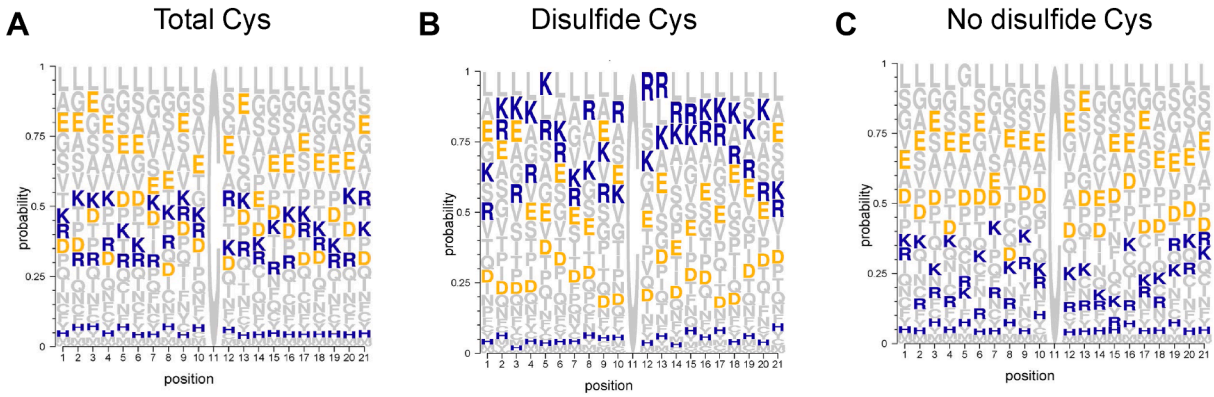

	Average (%)	Disulfide Cys (%)	No disulfide Cys (%)
Leu	9.10	9.95	9.13
Arg			
overall	5.10	8.42	4.12
+1 position	5.93	12.60	3.68
+2 position	5.63	10.79	3.70
Lys	5.80	7.75	4.62
His	2.20	2.03	2.60
Glu	6.20	6.65	6.99
Asp	5.30	4.67	5.57

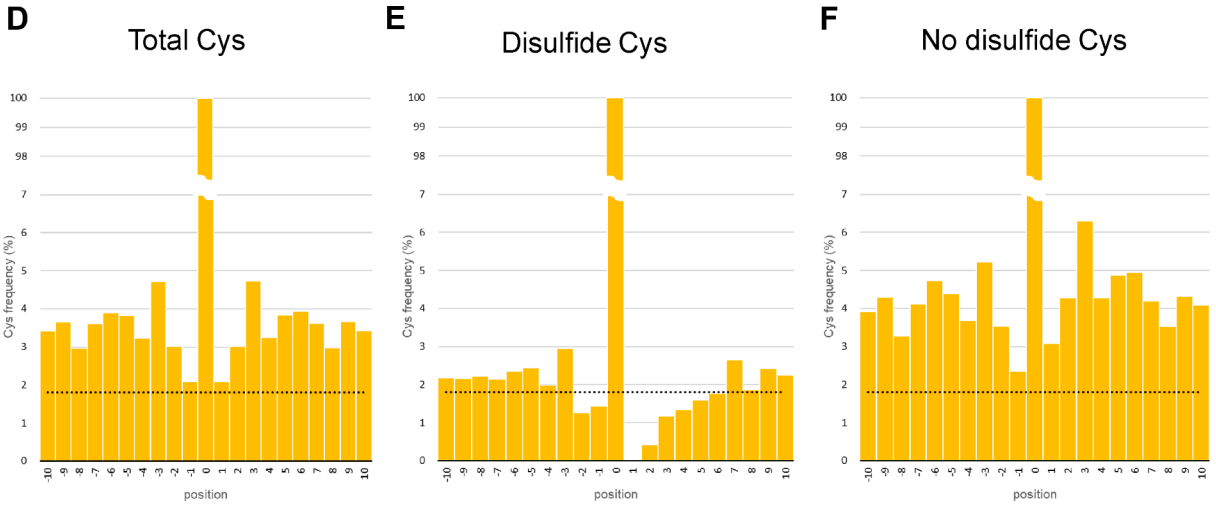

FIG. 8. **Amino acid frequencies near Cys residues**. *A* and *C*, amino acid frequencies at positions ±10 around Cys residues, categorized as (*A*) all Cys residues, (*B*) disulfide-forming Cys residues, and (*C*) non-disulfide Cys residues. Positively charged amino acids (Lys, Arg) are shown in *blue*, while negatively charged amino acids (Asp, Glu) are shown in *yellow*. *D* and *F*, frequencies of Cys residues in each category. The *dotted lines* indicate the average proportion of Cys residues.

integrity for accurate redox proteome profiling. Also, the presence of diverse and reproducible PTMs in secondary bands with sufficient abundance implies that low-abundance secondary bands may also contain multiple modified proteoforms, even though their PTMs cannot be confidently assigned under current analytical constraints (19, 33, 34). Several "moonlighting" proteins such as GAPDH, PRDX1, and enolase exhibited extensive PTM remodeling and redox-

driven functional shifts (35). A representative example is glyceraldehyde-3-phosphate dehydrogenase (GAPDH), a key glycolytic enzyme that forms an intramolecular disulfide between catalytic cysteines upon H_2O_2-induced oxidation, leading to reversible enzyme inactivation. This redox-dependent inactivation transiently diverts glycolytic flux toward the pentose phosphate pathway, thereby increasing NADPH production and buffering oxidative stress (36). In addition to its glycolytic role, GAPDH has been reported to interact with RNA splicing complexes like p54nrb–PSF(16, 28). PRDX1 alternated between peroxidase and chaperone activities depending on redox state (8, 37, 38), while enolase one was implicated in mRNA stability regulation (39, 40). HSP60/HSP10 chaperonin complexes protected mitochondria from oxidative injury (41), and HSP27 formed Cys137-linked dimers associated with chemoresistance (42). Although their precise functional relevance remains to be determined, the consistent appearance of multiple redox-dependent bands suggests that even low-abundance secondary proteoforms could represent meaningful redox variants rather than technical artifacts (43) (Fig. 3). In contrast, most metabolic enzymes showed minimal banding and TMT changes, suggesting restricted redox responsiveness.

Our disulfide mapping also revealed novel disulfide-mediated inter-protein interactions. Examples include HSP70–β4-spectrin complexes and disulfide-linked apolipoproteins (44). STRING analysis revealed that while some subclusters shared known GO terms, others lacked annotated connections, implying previously uncharacterized interaction networks (Fig. 5, *B–C*). Novel disulfide bridges between EGFR and vascular endothelial growth factor receptor 2 or pyruvate dehydrogenase E1 subunit beta (ODPB/PDHB) suggest redox-dependent crosstalk between signaling and metabolic pathways (Fig. 5*B*) (45, 46). Similarly, TITIN and SSPO—large, disulfide-rich proteins—formed networks enriched in cell cycle or structural assembly functions, indicating that disulfide bonding can organize coordinated functional modules (data not shown).

Isoform-specific disulfide formation, as seen in 14-3-3 proteins, reinforces the idea that protein-protein interactions and redox modifications are context-dependent, and not solely dictated by primary sequence (Fig. 7). While ACTN1 and ACTN4 colocalized at stress fibers and invadopodia, only ACTN4 regulated invadopodia formation and ERα activity (47–50). Disulfide-linked interactomes of 14-3-3 isoforms also differed, with unique Cys mediating distinct bonds (Fig. 7*A*) (51–53). Despite nearly identical local sequences, disulfide patterns diverged—suggesting cellular environment and PTMs, not just sequence, determine isoform specificity. This principle is demonstrated by Nm23-H1 and Nm23-H2, isoforms of NDPK. Nm23-H1 formed a stress-induced Cys4–Cys145 disulfide that triggered hexamer dissociation and inactivation, whereas Nm23-H2, lacking Cys4, remained unaffected (6, 7, 30, 54).

Although AlphaFold (https://alphafold.ebi.ac.uk/) and crystal structures provide static insights, they fail to capture these redox-specific differences (55). This highlights that dynamic redox environments and PTMs are crucial determinants of disulfide formation and function. Our sequence analysis further supports this, showing selective enrichment of basic residues near redox-prone Cys residues (Fig. 8*A*) (23). However, not all C x K/R motifs formed disulfides, indicating additional layers of regulation.

Despite the scope of this work, several limitations should be acknowledged. The peptide-level ambiguity in disulfide assignment–particularly for sequences conserved among homologs or distinct proteins–posed challenges in protein-specific interpretation. For example, ERACYLSINPQK was shared by α-/β-centractin, and CLSSLK appeared in three unrelated proteins—6-phosphogluconate dehydrogenase, the transcription factor HIVEP2, and the E3 ligase Nedd4—complicating protein assignment. These unspecific peptides were excluded from network visualizations using the neXtProt Peptide Uniqueness Checker to maintain data accuracy. Furthermore, while AlphaFold predictions and static crystal structures provided useful reference points, they failed to account for redox-dependent conformational changes, underscoring the need for dynamic structural analyses under oxidative conditions.

Several studies have previously mapped the H_2O_2-responsive redox proteome. Chemoproteomic profiling by Fu *et al*. (56) identified cysteine residues undergoing selective oxidation, whereas Baty *et al*. (57) used 2D electrophoresis to capture a limited subset of thiol-modified proteins. van der Reest *et al*. (58) further demonstrated how redox perturbation rewires metabolic flux by linking proteomic and metabolomics changes.

In contrast to strategies that rely on thiol-labeling or reducing workflows, our non-reducing proteomics approach preserved native disulfide states, enabling direct detection of disulfide-linked protein complexes and redox-driven shifts in apparent molecular mass. This unique structural context allowed us to uncover isoform-dependent disulfide selectivity, identify low-abundance proteoforms captured only under oxidizing conditions, and connect these disulfide events to functional metabolic adaptation through parallel metabolomics.

To translate these findings into biological or clinical insights, future work should investigate the functional consequences of individual disulfide bonds *in vivo*. Time-resolved redox proteomics and structural dynamics under oxidative stress will help elucidate the regulatory logic of disulfide network formation. Furthermore, integrating these redox-specific networks with transcriptomic or metabolomics data may reveal how oxidative stress reprograms cellular systems at multiple levels.

Collectively, this study advances redox proteomics by comprehensively identifying redox-sensitive proteins and disulfide-linked interactions under non-reducing conditions.

Our findings reveal that disulfide bonds are selective, biologically meaningful modifications that organize signaling, metabolic, and structural networks—particularly in isoform-specific contexts. These results offer a foundation for further exploration of Cys-dependent regulation and redox-controlled protein networks in health and disease.

DATA AVAILABILITY

The mass spectrometry proteomics data have been deposited to the ProteomeXchange Consortium via the MassIVE partner repository with the dataset identifier PXD070200 (MassIVE ID: MSV000099722_reviewer).

Reviewer access: ftp://MSV000099722@massive-ftp.ucsd.edu (password: 1106).

The Metabolmics dataset is available at the following DOI: https://doi.org/10.5281/zenodo.17585755.

Supplemental Data—This article contains supplemental data.

Acknowledgments—This work was supported by a National Research Foundation of Korea (NRF) grant funded by the Ministry of Science and ICT (RS-2024-00338237 to E. J. S.) and Korea Basic Science Institute (National Research Facilities and Equipment Center) grant funded by the Ministry of Education (2021R1A6C101A442 to E. J. S.). This work is additionally funded by the Korea Basic Science Institute (C523400 to S. N.).

Author Contributions—Y. L., S. N., K. J. L., J. J., and E. J. S. writing– review and editing; Y. L. writing–original draft; Y. L. visualization; Y. L., T. K. K., and J. J., investigation; Y. L., T. K. K., and K. J. L. conceptualization; T. K. K. and K. J. L. supervision; S. N. methodology.

Conflictof Interest—The authors declare no competing interests.

Abbreviations—The abbreviations used are: ACN, Acetonitrile; ACTN, alpha-actinin; Cys, cysteine; emPAI, exponentially modified protein abundance index; GO, gene gntology; H_2O_2, hydrogen peroxide; ROS, reactive oxygen species; PPP, pentose phosphate pathway; PRDX, peroxiredoxin; PRDX1, peroxiredoxin 1; PRPP, phosphoribosyl pyrophosphate; PTM, post-translational modification; SDH, succinate dehydrogenase; SSPO, SCO-spondin; TCA, tricarboxylic acid; TMT, tandem mass tag.

Received September 1, 2025, and in revised form, February 11, 2026 Published, MCPRO Papers in Press, March 2, 2026, https://doi.org/10.1016/j.mcpro.2026.101548

REFERENCES

1. Kim, Y. M., Kim, K. E., Koh, G. Y., Ho, Y. S., and Lee, K. J. (2006) Hydrogen peroxide produced by angiopoietin-1 mediates angiogenesis. *Cancer Res.* **66**, 6167–6174
2. Ahn, J. H., Cho, M. G., Basit, A., Song, I. K., Lee, K. J., and Lee, J. H. (2025) Cdk1-dependent lamin aggregation underlies oxidative stress-induced nuclear shape abnormalities. *BMB Rep.* **59**, 69–77
3. Rhee, S. G. (2006) Cell signaling. H2O2, a necessary evil for cell signaling. *Science* **312**, 1882–1883
4. Ray, P. D., Huang, B. W., and Tsuji, Y. (2012) Reactive oxygen species (ROS) homeostasis and redox regulation in cellular signaling. *Cell Signal.* **24**, 981–990
5. Truong, T. H., and Carroll, K. S. (2012) Redox regulation of epidermal growth factor receptor signaling through cysteine oxidation. *Biochemistry* **51**, 9954–9965
6. Lee, E., Jeong, J., Kim, S. E., Song, E. J., Kang, S. W., and Lee, K. J. (2009) Multiple functions of Nm23-H1 are regulated by oxido-reduction system. *PLoS One* **4**, e7949
7. Kim, M. S., Jeong, J., Jeong, J., Shin, D. H., and Lee, K. J. (2013) Structure of Nm23-H1 under oxidative conditions. *Acta Crystallogr. D Biol. Crystallogr.* **69**, 669–680
8. Song, I. K., Lee, J. J., Cho, J. H., Jeong, J., Shin, D. H., and Lee, K. J. (2016) Degradation of redox-sensitive proteins including peroxiredoxins and DJ-1 is promoted by oxidation-induced conformational changes and ubiquitination. *Sci. Rep.* **6**, 34432
9. Giles, N. M., Watts, A. B., Giles, G. I., Fry, F. H., Littlechild, J. A., and Jacob, C. (2003) Metal and redox modulation of cysteine protein function. *Chem. Biol.* **10**, 677–693
10. Salsbury, F. R., Jr., Knutson, S. T., Poole, L. B., and Fetrow, J. S. (2008) Functional site profiling and electrostatic analysis of cysteines modifiable to cysteine sulfenic acid. *Protein Sci.* **17**, 299–312
11. Jeong, J., Jung, Y., Na, S., Jeong, J., Lee, E., Kim, M. S., *et al*. (2011) Novel oxidative modifications in redox-active cysteine residues. *Mol. Cell Proteomics* **10**, M110.000513
12. Choi, S., Jeong, J., Na, S., Lee, H. S., Kim, H. Y., Lee, K. J., *et al*. (2010) New algorithm for the identification of intact disulfide linkages based on fragmentation characteristics in tandem mass spectra. *J. Proteome Res.* **9**, 626–635
13. Lee, J. J., Ha, S., Kim, H. J., Ha, H. J., Lee, H. Y., and Lee, K. J. (2014) Sulfhydryl-specific probe for monitoring protein redox sensitivity. *ACS Chem. Biol.* **9**, 2883–2894
14. Song, I. K., Kim, M. S., Ferrell, J. E., Jr., Shin, D. H., and Lee, K. J. (2021) Stepwise oxidations play key roles in the structural and functional regulations of DJ-1. *Biochem. J.* **478**, 3505–3525
15. Qvit, N., Joshi, A. U., Cunningham, A. D., Ferreira, J. C., and Mochly-Rosen, D. (2016) Glyceraldehyde-3-Phosphate dehydrogenase (GAPDH) protein-protein interaction inhibitor reveals a non-catalytic role for GAPDH oligomerization in cell death. *J. Biol. Chem.* **291**, 13608–13621
16. Hwang, N. R., Yim, S. H., Kim, Y. M., Jeong, J., Song, E. J., Lee, Y., *et al*. (2009) Oxidative modifications of glyceraldehyde-3-phosphate dehydrogenase play a key role in its multiple cellular functions. *Biochem. J.* **423**, 253–264
17. Hoffmann, J. H., Linke, K., Graf, P. C., Lilie, H., and Jakob, U. (2004) Identification of a redox-regulated chaperone network. *EMBO J.* **23**, 160–168
18. Peterson, A. L., Walker, A. K., Sloan, E. K., and Creek, D. J. (2016) Optimized method for untargeted metabolomics analysis of MDA-MB-231 breast cancer cells. *Metabolites* **6**, 30
19. Echan, L. A., and Speicher, D. W. (2002) Protein detection in gels using fixation. *Curr. Protoc. Protein Sci.* **10**, 15.11-10.15.18
20. Shannon, P., Markiel, A., Ozier, O., Baliga, N. S., Wang, J. T., Ramage, D., *et al*. (2003) Cytoscape: a software environment for integrated models of biomolecular interaction networks. *Genome Res.* **13**, 2498–2504
21. Forshaw, T. E., Holmila, R., Nelson, K. J., Lewis, J. E., Kemp, M. L., Tsang, A. W., *et al*. (2019) Peroxiredoxins in cancer and response to radiation therapies. *Antioxidants (Basel)* **8**, 11
22. Ishihama, Y., Oda, Y., Tabata, T., Sato, T., Nagasu, T., Rappsilber, J., *et al*. (2005) Exponentially modified protein abundance index (emPAI) for estimation of absolute protein amount in proteomics by the number of sequenced peptides per protein. *Mol. Cell Proteomics* **4**, 1265–1272
23. Xiao, H., Jedrychowski, M. P., Schweppe, D. K., Huttlin, E. L., Yu, Q., Heppner, D. E., *et al*. (2020) A quantitative tissue-specific landscape of protein redox regulation during aging. *Cell* **180**, 968–983.e924
24. Agrawal, K., Asthana, S., and Kumar, D. (2023) Role of oxidative stress in metabolic reprogramming of brain cancer. *Cancers (Basel)* **15**, 4920

25. Lin, R., Elf, S., Shan, C., Kang, H. B., Ji, Q., Zhou, L., *et al*. (2015) 6-Phosphogluconate dehydrogenase links oxidative PPP, lipogenesis and tumour growth by inhibiting LKB1-AMPK signalling. *Nat. Cell Biol.* **17**, 1484–1496
26. Bhardwaj, V., and He, J. (2020) Reactive oxygen species, metabolic plasticity, and drug resistance in cancer. *Int. J. Mol. Sci.* **21**, 3412
27. Pandolfi, P. P., Sonati, F., Rivi, R., Mason, P., Grosveld, F., and Luzzatto, L. (1995) Targeted disruption of the housekeeping gene encoding glucose 6-phosphate dehydrogenase (G6PD): G6PD is dispensable for pentose synthesis but essential for defense against oxidative stress. *EMBO J.* **14**, 5209–5215
28. Sirover, M. A. (2018) Pleiotropic effects of moonlighting glyceraldehyde-3-phosphate dehydrogenase (GAPDH) in cancer progression, invasiveness, and metastases. *Cancer Metastasis Rev.* **37**, 665–676
29. Chen, Y. R., Chen, C. L., Pfeiffer, D. R., and Zweier, J. L. (2007) Mitochondrial complex II in the post-ischemic heart: oxidative injury and the role of protein S-glutathionylation. *J. Biol. Chem.* **282**, 32640–32654
30. Kim, B., and Lee, K. J. (2021) Activation of Nm23-H1 to suppress breast cancer metastasis via redox regulation. *Exp. Mol. Med.* **53**, 346–357
31. Kim, B., Lee, J. J., Shin, J. S., Suh, J. W., Jung, S., Hwang, G. S., *et al*. (2021) Nm23-H1 activator phenylbutenoid dimer exerts cytotoxic effects on metastatic breast cancer cells by inducing mitochondrial dysfunction only under glucose starvation. *Sci. Rep.* **11**, 23549
32. Takénaka, A., and Moras, D. (2020) Correlation between equi-partition of aminoacyl-tRNA synthetases and amino-acid biosynthesis pathways. *Nucleic Acids Res.* **48**, 3277–3285
33. Fonslow, B. R., Carvalho, P. C., Academia, K., Freeby, S., Xu, T., Nakorchevsky, A., *et al*. (2011) Improvements in proteomic metrics of low abundance proteins through proteome equalization using ProteoMiner prior to MudPIT. *J. Proteome Res.* **10**, 3690–3700
34. Carbonara, K., Andonovski, M., and Coorssen, J. R. (2021) Proteomes are of proteoforms: embracing the complexity. *Proteomes* **9**, 38
35. Gupta, M. N., and Uversky, V. N. (2023) Moonlighting enzymes: when cellular context defines specificity. *Cell. Mol. Life. Sci.* **80**, 130
36. Talwar, D., Miller, C. G., Grossmann, J., Szyrwiel, L., Schwecke, T., Demichev, V., *et al*. (2023) The GAPDH redox switch safeguards reductive capacity and enables survival of stressed tumour cells. *Nat. Metab.* **5**, 660–676
37. Bolduc, J., Koruza, K., Luo, T., Malo Pueyo, J., Vo, T. N., Ezeriņa, D., *et al*. (2021) Peroxiredoxins wear many hats: factors that fashion their peroxide sensing personalities. *Redox Biol.* **42**, 101959
38. Hoyle, N. P., and O'Neill, J. S. (2015) Oxidation-reduction cycles of peroxiredoxin proteins and nontranscriptional aspects of timekeeping. *Biochemistry* **54**, 184–193
39. Morita, T., Kawamoto, H., Mizota, T., Inada, T., and Aiba, H. (2004) Enolase in the RNA degradosome plays a crucial role in the rapid decay of glucose transporter mRNA in the response to phosphosugar stress in Escherichia coli. *Mol. Microbiol.* **54**, 1063–1075
40. Qiao, G., Wu, A., Chen, X., Tian, Y., and Lin, X. (2021) Enolase 1, a moonlighting protein, as a potential target for cancer treatment. *Int. J. Biol. Sci.* **17**, 3981–3992
41. Lin, K. M., Lin, B., Lian, I. Y., Mestril, R., Scheffler, I. E., and Dillmann, W. H. (2001) Combined and individual mitochondrial HSP60 and HSP10 expression in cardiac myocytes protects mitochondrial function and prevents apoptotic cell deaths induced by simulated ischemia-reoxygenation. *Circulation* **103**, 1787–1792
42. Choi, B., Choi, S. K., Park, Y. N., Kwak, S. Y., Lee, H. J., Kwon, Y., *et al*. (2017) Sensitization of lung cancer cells by altered dimerization of HSP27. *Oncotarget* **8**, 105372–105382
43. Drown, B. S., Jooß, K., Melani, R. D., Lloyd-Jones, C., Camarillo, J. M., and Kelleher, N. L. (2022) Mapping the proteoform landscape of five human tissues. *J. Proteome Res.* **21**, 1299–1310
44. Cumming, R. C., Andon, N. L., Haynes, P. A., Park, M., Fischer, W. H., and Schubert, D. (2004) Protein disulfide bond formation in the cytoplasm during oxidative stress. *J. Biol. Chem.* **279**, 21749–21758
45. Paul, M. D., and Hristova, K. (2021) Interactions between ligand-bound EGFR and VEGFR2. *J. Mol. Biol.* **433**, 167006
46. Han, Z., Zhong, L., Srivastava, A., and Stacpoole, P. W. (2008) Pyruvate dehydrogenase complex deficiency caused by ubiquitination and proteasome-mediated degradation of the E1 subunit. *J. Biol. Chem.* **283**, 237–243
47. Yamaguchi, H., Ito, Y., Miura, N., Nagamura, Y., Nakabo, A., Fukami, K., *et al*. (2017) Actinin-1 and actinin-4 play essential but distinct roles in invadopodia formation by carcinoma cells. *Eur. J. Cell Biol.* **96**, 685–694
48. Misiura, M., Zińczuk, J., Zaręba, K., Kamińska, D., Guzińska-Ustymowicz, K., and Pryczynicz, A. (2020) Actin-bundling proteins (Actinin-4 and Fascin-1) are involved in the development of pancreatic intraepithelial neoplasia (PanIN). *Am. J. Med. Sci.* **359**, 147–155
49. Yamamoto, S., Tsuda, H., Honda, K., Onozato, K., Takano, M., Tamai, S., *et al*. (2009) Actinin-4 gene amplification in ovarian cancer: a candidate oncogene associated with poor patient prognosis and tumor chemoresistance. *Mod. Pathol.* **22**, 499–507
50. Khurana, S., Chakraborty, S., Cheng, X., Su, Y. T., and Kao, H. Y. (2011) The actin-binding protein, actinin alpha 4 (ACTN4), is a nuclear receptor coactivator that promotes proliferation of MCF-7 breast cancer cells. *J. Biol. Chem.* **286**, 1850–1859
51. Sengupta, A., Liriano, J., Bienkiewicz, E. A., Miller, B. G., and Frederich, J. H. (2020) Probing the 14-3-3 isoform-specificity profile of protein-protein interactions stabilized by Fusicoccin A. *ACS Omega.* **5**, 25029–25035
52. Kim, M. K., Cho, J. H., Lee, J. J., Son, M. H., and Lee, K. J. (2015) Proteomic analysis of INS-1 rat insulinoma cells: ER stress effects and the protective role of exenatide, a GLP-1 receptor agonist. *PLoS One* **10**, e0120536
53. Betters, R. K., Luhmann, E., Gottschalk, A. C., Xu, Z., Shin, M. R., Ptak, C. P., *et al*. (2023) Characterization of the Tau interactome in human brain reveals isoform-dependent interaction with 14-3-3 family proteins. *eNeuro* **10**, ENEURO.0503-22.2023
54. Lee, J. J., Kim, H. S., Lee, J. S., Park, J., Shin, S. C., Song, S., *et al*. (2018) Small molecule activator of Nm23/NDPK as an inhibitor of metastasis. *Sci. Rep.* **8**, 10909
55. Terwilliger, T. C., Liebschner, D., Croll, T. I., Williams, C. J., McCoy, A. J., Poon, B. K., *et al*. (2024) AlphaFold predictions are valuable hypotheses and accelerate but do not replace experimental structure determination. *Nat. Methods* **21**, 110–116
56. Fu, L., Liu, K., Sun, M., Tian, C., Sun, R., Morales Betanzos, C., *et al*. (2017) Systematic and quantitative assessment of hydrogen peroxide reactivity with cysteines across human proteomes. *Mol. Cell Proteomics* **16**, 1815–1828
57. Baty, J. W., Hampton, M. B., and Winterbourn, C. C. (2005) Proteomic detection of hydrogen peroxide-sensitive thiol proteins in Jurkat cells. *Biochem. J.* **389**, 785–795
58. van der Reest, J., Lilla, S., Zheng, L., Zanivan, S., and Gottlieb, E. (2018) Proteome-wide analysis of cysteine oxidation reveals metabolic sensitivity to redox stress. *Nat. Commun.* **9**, 1581